



# Scalable electrodeposition of NiFe-based electrocatalysts with self-evolving multi-vacancies for high-performance industrial water electrolysis

Zhuoming Wei <sup>a</sup>, Mengwei Guo <sup>a</sup>, Qibo Zhang <sup>a,b,\*</sup>

<sup>a</sup> Key Laboratory of Ionic Liquids Metallurgy, Faculty of Metallurgical and Energy Engineering, Kunming University of Science and Technology, Kunming 650093, PR China

<sup>b</sup> State Key Laboratory of Complex Nonferrous Metal Resources Cleaning Utilization in Yunnan Province, Kunming 650093, PR China



## ARTICLE INFO

### Keywords:

Deep eutectic solvent  
NiFe-based electrocatalysts  
Multi-vacancies  
Electrodeposition  
AEM water electrolysis

## ABSTRACT

Water electrolysis is a promising technique for green hydrogen production to achieve the global strategic goal of carbon neutrality. Herein, we propose an optimized-electrodeposition set-up in Ethaline-based deep eutectic solvent (DES) for the electrochemical preparation of NiFe-based catalysts. The developed synthesis procedure involves the anodic dissolution of Fe plates to provide Fe sources, which are gradually incorporated into the in-situ grown Ni films to fabricate NiFe-based electrodes. Our findings show that introducing nitrate ions coupled with electrochemical water oxidation can induce the formation of multi-vacancy-rich NiFe-based catalysts with outstanding water splitting performance in quasi-industrial conditions. A simulated industrial anion exchange membrane (AEM)-based device loaded with our NiFe-based electrocatalysts requires only 1.73 V<sub>cell</sub> to reach 1000 mA cm<sup>-2</sup> in 5.0 M KOH at 60 °C and works continuously for up to 200 h. The present work provides a means for the scalable synthesis of self-supported NiFe-based catalysts for industrial water splitting.

## 1. Introduction

Hydrogen production via electrochemical water splitting powered by renewable electricity input is a promising approach to address the issues of energy depletion and environmental pollution [1]. Nonetheless, due to the high kinetic and thermodynamic barrier of the two semi-reactions: four-electron-transfer for oxygen evolution reaction (OER) and two-electron-transfer for hydrogen evolution reaction (HER), high-performance catalysts are required to accelerate the overall reaction process at lower overpotentials [2]. Precious metals and their oxides, such as Pt-based and Ru/Ir-based oxide catalysts, have satisfactory HER and OER catalytic performance. However, their high cost and limited reserves restrict their utility for industrial applications [3]. The rational development of high-efficiency, low-cost precious metal-free catalysts for industrial applications remains a crucial challenge.

Industrial water electrolysis electrolyzers can be mainly divided into proton exchange membrane water electrolysis (PEMWE), alkaline water electrolysis (AWE), solid polymer anion exchange membrane water electrolysis (AEMWE), and solid oxide electrolysis (SOE) based on the operating temperature and electrolyte nature [4]. Only PEMWE and AWE are successfully applied in industrial production. However, the

conventional porous diaphragm structure of AWE requires a pressure balance between the anode and cathode compartments to prevent the mixing of the hydrogen and oxygen gases produced in the two compartments, leading to low operational efficiency and reduced hydrogen purity. For hydrogen production using PEMWE, the system operates at low pH, requiring precious metal-based catalysts and titanium bipolar plates to improve efficiency and longevity, resulting in high manufacturing costs [5]. Compared to PEMWE, AEMWE offers the leverage advantages of catalytic materials, which are cheaper and less susceptible to acid corrosion [6]. Furthermore, AEMWE also facilitates rapid load fluctuations compared to AWE and is compatible with the high volatility and stochasticity of wind and solar power generation [7], making it a promising advanced water electrolysis technology for hydrogen production. For efficient hydrogen production, catalysts should be able to operate stably at high current densities (> 500 mA cm<sup>-2</sup>) under harsh conditions such as high temperature (60–90 °C), high electrolyte concentration (20–30 wt% alkaline), and high pressure (6–200 bar) to meet the practical needs of industrial water electrolysis, but there are few relevant studies [8,9]. Lab-fabricated catalytic materials need to stand the test of industrial conditions before being promoted to practical applications.

\* Correspondence to: Key Laboratory of Ionic Liquids Metallurgy, Faculty of Metallurgical and Energy Engineering, Kunming University of Science and Technology, No.68 WenChang Road, 121 Street, Kunming 650093, PR China.

E-mail address: [qibozhang@kust.edu.cn](mailto:qibozhang@kust.edu.cn) (Q. Zhang).

NiFe-based materials have emerged as promising alternatives to replace the precious-metal-based catalysts due to their economical cost and outstanding performance in OER and HER [10,11]. Among them, NiFe-based (oxy)hydroxide materials are widely investigated as high-efficiency and low-cost OER electrocatalysts [2]. It is confirmed that  $\text{Fe}^{4+}$  species in-situ generated from iron hydroxides are positively correlated with the OER performance of NiFe (oxy)hydroxide [12]. Additionally, the synergy between  $\text{Fe}(\text{OH})_2/\text{FeOOH}$  and  $\text{Ni}(\text{OH})_2/\text{NiOOH}$  contributes to the enhanced catalytic activity [13]. Further improvement in the OER catalytic performance of NiFe-based electrocatalysts could be achieved by constructing smart structures and hybrid composites [14]. Impressively, NiFe-based OER catalysts can be further converted to HER catalysts via phosphatization treatment with the introduction of P, which showed high HER activity comparable to commercial Pt/C catalysts [15]. The doping of P can induce strong electron interaction and promote electron transfer to accelerate the reaction kinetics and thus boost the overall water splitting activity [16]. Despite some progress for NiFe-based catalysts, most research remains confined to the small-scale laboratory stage, different from industrial application conditions [17]. The practical application of these catalysts requires their being firmly grafted onto the current collector to function stably at high current density under harsh industrial conditions. Some pioneering works have attempted to prepare integrated NiFe-based electrodes with self-supported architectures as efficient catalysts for high-current-density water splitting under a simulated industrial environment. Zou et al. [18] proposed a wet chemistry approach to efficiently prepare amorphous Ni-Fe bimetallic hydroxide (NiFe-OH) films developed on the  $\text{Ni}_3\text{S}_2$  nanosheet arrays that in-situ growth on nickel foam (NF), which showed high OER catalytic performance at an industrial-grade current density of  $1 \text{ A cm}^{-2}$  in 30 wt% KOH. In addition, regulable corrosion engineering of Fe substrates, such as Fe foil, Fe foam, and spent stainless steel, has recently been employed to prepare self-supported Ni-Fe-based OER electrocatalysts [19,20]. The robust structural feature of these self-supported materials enables them as high-current-density electrodes for efficient water splitting. However, few reports involved assembling water electrolysis devices with lab-prepared NiFe-based materials and further evaluating their installation performance under industrial conditions. The creative design and facile synthesis of NiFe-based catalytic materials with industrial application prospects need further exploration.

In this work, we developed a scalable electrodeposition route for the fabrication of NiFe-based catalysts in Ethaline-based DES using a sacrificial anode set-up. Both Ni-Fe and Ni-Fe-P catalytic electrodes are synthesized via a facile, one-step electrodeposition approach by simply adjusting the composition of the electrolyte. Compared with commonly used inert anodes, the introduction of Fe anodes can provide Fe sources and regulate the electrodeposition process to significantly reduce the cell voltage required (energy consumption). In this manner, the potential system decomposition and the contamination of inert anode at high potential during the electrodeposition process are expected to be significantly reduced via the dissolution of the anode itself [21]. The introduction of  $\text{NO}_3^-$  ions with nickel nitrate as the Ni source is observed to induce different morphologies and result in the formation of the Ni-Fe hybrid catalysts rich in multi-vacancies during the OER process as compared to the chloride counterparts. Facilitated by the proliferative multi-vacancies, the fabricated Ni-Fe hybrid electrocatalysts exhibited outstanding catalytic performance towards water splitting under quasi-industrial conditions. The integration of our fabricated Ni-Fe hybrid catalysts (with an effective area of  $10 \text{ cm}^2$ ) into a simulated AEM electrolysis device showed good installation performance, requiring only  $1.73 \text{ V}_{\text{cell}}$  to drive  $1000 \text{ mA cm}^{-2}$  in  $5.0 \text{ M KOH}$  at  $60^\circ\text{C}$ . The assembly system can work steadily for up to 200 h, promising for large-scale industrial applications.

## 2. Experimental section

### 2.1. Materials and reagents

Nickel nitrate tetrahydrate ( $\text{Ni}(\text{NO}_3)_2 \cdot 4\text{H}_2\text{O}$ ,  $\geq 98\%$ ), nickel chloride hexahydrate ( $\text{NiCl}_2 \cdot 6\text{H}_2\text{O}$ ,  $\geq 98\%$ ), iron chloride hexahydrate ( $\text{FeCl}_3 \cdot 6\text{H}_2\text{O}$ ,  $\geq 98\%$ ), sodium hypophosphite ( $\text{NaH}_2\text{PO}_2$ ,  $\geq 99\%$ ), choline chloride ( $\text{ChCl}$ ,  $\geq 99\%$ ), potassium hydroxide ( $\text{KOH}$ ,  $\geq 99\%$ ), ethylene glycol (EG,  $\geq 99\%$ ) and deionized water ( $>18 \text{ M}\Omega \text{ cm}^{-1}$ ) were analytically pure and purchased from Aladdin Reagent Ltd. High purity Fe plate (99.99 %) and commercial Cu foam were bought from Jinding Metal Material Co, Ltd (Hebei, China). Fumasep FAA-3-PE-30 (a commercial PE-reinforced anion exchange membrane) was obtained from FuMA-Tech (Germany). The Ethaline-based DES was synthesized by blending ChCl and EG in a flask at a 1:2 molar ratio. The mixture was then stirred at 353 K until it became homogeneous and the translucent liquid formed [21].

### 2.2. Electrodeposition preparation of NiFe-based catalysts

NiFe-based hybrid catalysts were prepared in Ethaline-based DES via a simple and scalable one-step galvanostatic electrodeposition process controlled by a power supply at a current density of  $2 \text{ mA cm}^{-2}$ . Different from the common co-deposition model, herein Fe is gradually introduced by Fe sacrificing anode. In contrast, Ni is introduced by adding Ni salts (either  $\text{Ni}(\text{NO}_3)_2 \cdot 4\text{H}_2\text{O}$  or  $\text{NiCl}_2 \cdot 6\text{H}_2\text{O}$ ) into the target electrolyte. Prior to each deposition, the Cu foam and Fe plate were ultrasonically washed with acetone and  $0.1 \text{ M HCl}$  solution for 5 min before each deposition to remove surface oxide layers. In a typical synthesis, the galvanostatic electrodeposition process was carried out on a commercial Cu foam with two parallel-arranged Fe plates serving as the anodes from the Ethaline-based DES containing  $10 \text{ mM Ni}$  salt at 353 K. To optimize the electrodeposition process, the applied current density, the amount of charge and set-up were systematically varied, according to the resultant catalytic performance of the prepared NiFe-based electrodes. After deposition, the prepared catalysts were rinsed with ethanol and deionized water and then dried in the air.

For facile distinction, the NiFe catalyst obtained from the electrolyte containing  $\text{Ni}(\text{NO}_3)_2 \cdot 4\text{H}_2\text{O}$  with the set-up of Fe anode is recorded as NiFe\_FA\_NN and the sample prepared from the electrolyte containing  $\text{NiCl}_2 \cdot 6\text{H}_2\text{O}$  with the same set-up is denoted as NiFe\_FA\_NC. P doping can be easily achieved by adding additional  $\text{NaH}_2\text{PO}_2$  (5 mM) into the electrolyte with a similar procedure. Similarly, depending on the anode materials and Ni salts used, the resulting samples are labeled as NiFeP\_FA\_NN and NiFeP\_FA\_NC, respectively. For a direct comparison, the counterparts, including NiFe\_GA\_NN and NiFeP\_GA\_NN, were fabricated from the electrolyte containing  $\text{Ni}(\text{NO}_3)_2 \cdot 4\text{H}_2\text{O}$  and  $\text{FeCl}_3 \cdot 6\text{H}_2\text{O}$  with graphite plate as the anode, and the NiFe\_GA\_NC and NiFeP\_GA\_NC were obtained by further replacing the Ni source with  $\text{NiCl}_2 \cdot 6\text{H}_2\text{O}$ . To simulate the solvent environment of Fe anode set-up, the addition amount of  $\text{FeCl}_3 \cdot 6\text{H}_2\text{O}$  is set to be half of the Ni salt.

### 2.3. Characterization

Scanning electron microscopic (SEM) was performed on a field emission scanning electron microscope (NOVA Nano SEM 450) with a 15 kV accelerating voltage. The transmission electron microscope (TEM) characterizations were carried out on a Tecnai G2 F30 transmission electron microscope that was coupled with an energy dispersive X-ray spectrometer (EDX). X-ray diffraction (XRD) conducted on a Rigaku X-ray diffractometer (Minifex II Desktop) was used to characterize the crystal structure of the as-prepared catalysts. An X-ray photoelectron spectrometer (XPS, PHI 550) was used to investigate the chemical states on the surface. Photoluminescence (PL) spectra were collected with an excitation wavelength of 325 nm at room temperature to explore the defects formed in the prepared samples. Raman spectra were recorded

on a Raman spectrometer of Renishaw Invia Plus laser (Renishaw, UK) equipped with a 325 nm laser excitation source. Ni and Fe mass loadings on the substrate after electrodeposition were detected by inductively coupled plasma optical emission spectrometry (ICP-OES, PerkinElmer ELAN DRC-e, USA).

Ni K-edge analysis was carried out with Si(111) crystal monochromators at the BL11B beamlines of the Shanghai Synchrotron Radiation Facility (SSRF) characterization (Shanghai, China) for X-ray absorption fine structure (XAFS). Before analysis, samples were pressed into thin sheets of 1 cm diameter and sealed using Kapton tape film. The XAFS spectra were acquired at ambient temperature using a Bruker 5040 4-channel Silicon Drift Detector (SDD). Transmission spectra of Ni K-edge extended X-ray absorption fine structure (EXAFS) were obtained. Only negligible variations in the line shape and peak position of the Ni K-edge X-ray absorption near edge structure (XANES) spectra were observed between two scans of the same sample. For comparison, the XAFS spectra of typical Ni foil and NiO samples were collected.

#### 2.4. Electrochemical measurements

All electrochemical measurements mentioned subsequently were performed on a CHI 760E model electrochemical workstation (Chenhua Instrument, China) in 1.0 M KOH at 298 K or simulated industrial conditions of 5.0 M KOH at 353 K. A conventional three-electrode configuration was utilized, with the prepared sample serving as the working electrode, a graphite rod ( $\Phi = 5$  mm, length = 2 cm) and Hg/HgO (1.0 M KOH) electrode as the counter and reference electrodes, respectively. Prior to each measurement, high purity nitrogen was injected for at least 10 min to remove the oxygen dissolved in the solution. The anode and cathode polarization curves were conducted to evaluate the OER and HER performance of the prepared electrocatalysts, which were conducted at a scan rate of  $5 \text{ mV s}^{-1}$  from 0 V to  $-0.7 \text{ V}$  vs. RHE for HER and  $1.1\text{--}1.9 \text{ V}$  vs. RHE for OER. Electrochemical impedance spectroscopy (EIS) was carried out in the frequency range from  $10^5$  to  $10^{-2} \text{ Hz}$  at a given potential with an AC voltage amplitude of 5 mV. The electrochemical active surface area (ECSA) of the prepared electrodes was estimated by electrochemical double-layer capacitance ( $C_{dl}$ ) measurements according to a cyclic voltammogram (CV) method. CV scanning was performed at different scan rates from 10 to  $100 \text{ mV s}^{-1}$  in non-Faradaic regions to collect the capacitance charging and discharging currents. To avoid the influence of iR-compensation on evaluating the intrinsic catalytic performance of the as-prepared samples under simulated industrial conditions with a high current density, all the potentials presented in this work are without iR-compensation.

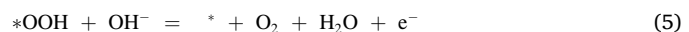
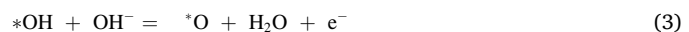
#### 2.5. DFT calculation detail

The Vienna Ab initio Simulation Package (VASP) was used for density functional theory (DFT) computations. The Perdew-Burke-Ernzerhof (PBE) generalized gradient approximation (GGA) exchange-correlation function was used with the projector augmented wave (PAW) pseudopotential. To accommodate for strongly localized p-electrons in Ni ( $\text{U}_{eff} = 6.2 \text{ eV}$ ) and Fe ( $\text{U}_{eff} = 5.3 \text{ eV}$ ), all metal oxide energetics were estimated using DFT with the Hubbard-U framework (DFT+U). The plane waves basis set has a cutoff energy of 500 eV, and a Monkhorst-Pack mesh of 331 was utilized in K-sampling to compute the adsorption energy. All structures were spin-polarized, and all atoms were completely relaxed with a tolerance of  $10\text{--}5 \text{ eV per atom}$  for energy convergence. The final force on each atom was  $< 0.05 \text{ eV \AA}^{-1}$ . The adsorption energy of reaction intermediates can be computed using the following Eq. (1):

$$\Delta G_{ads} = \Delta E_{DFT} + \Delta ZPE - T\Delta S \quad (1)$$

Where  $*$  presents the active site for the adsorption of intermediates. The  $\Delta G_{ads}$  ( $ads = \text{OH}^*, \text{O}^*, \text{and OOH}^*$ ) are Gibbs free energies of OER

intermediates. The  $\Delta E_{DFT}$  is the calculated DFT reaction energy,  $\Delta ZPE$  is the zero-point energy change, and  $\Delta S$  is the entropy change. In this work, the values of  $\Delta ZPE$  and  $\Delta S$  were acquired by vibration frequency calculation. The four Equations below can be used to compute the Gibbs free energy of the four reaction stages. (2)-(5):



### 3. Results and discussion

#### 3.1. Synthesis and structural investigation of electrocatalysts

The new-developed self-supported NiFe-based catalysts were synthesized via a facile, template-free electrodeposition approach with different anode set-ups in Ethaline-based DES, as schematically illustrated in Fig. 1. Herein, the NiFe and NiFeP catalysts obtained from the electrolyte containing nickel nitrate in the absence and presence of  $\text{NaH}_2\text{PO}_2$  with the electrodeposition set-up of the Fe plate anode are denoted as NiFe\_FA\_NN and NiFeP\_FA\_NN, respectively (see more details in the experimental section). Previous studies have shown that the unique solvent environment offered by Ethaline-based DES provides inherent advantages for the fabrication of nanostructured electrode materials with high activity through electrodeposition methodology [22,23]. However, most of these electrodeposition settings were mainly based on inert anodes, such as graphite and Ti-based anodes, resulting in the risk of system decomposition at the high anodic potential [21]. Instead of choosing a high-frequency inert anode, we updated the deposition settings with a soluble Fe plate anode as the feedstock. The Fe plate that is slowly anodically dissolved provides Fe ions for the following cathodic electrodeposition process and avoids the possibility of solvent decomposition. The electrodeposition process can be advanced at a much lower cell voltage after anodic substitution (Fig. S1). Notably, such a deposition model could also be designed for anodic digestion of soluble materials for electrochemical conversion to construct catalytic materials on the cathode [24].

The crystalline structures of NiFe\_FA\_NN and NiFeP\_FA\_NN were first examined by the thin-film XRD, as shown in Fig. 2a. The firm diffraction peaks of metallic Cu and soft but noticeable peaks for metallic Ni can be observed for NiFe\_FA\_NN, suggesting the features of poor crystallinity and low mass loading. The incorporation of Fe with a content of 11.4 at % in the deposit is confirmed by the corresponding EDX analysis (Fig. S2a). In contrast, the characteristic peaks of Ni are further weakened by the introduction of 3.2 at% P, indicating that the crystallinity of NiFeP\_FA\_NN is further reduced and tends to be amorphous. The associated EDX data show that P doping can promote the deposition of Ni, leading to a higher Ni/Fe ratio (Fig. S2b). Accordingly, the SEM images of NiFe\_FA\_NN and NiFeP\_FA\_NN reveal clearly that the entire Cu foam substrates are uniformly covered with a nanoparticle-assembled NiFe layer (Fig. 2b) and rough NiFeP with a porous configuration (Fig. 2c), respectively. The TEM images (Fig. 2d and e) obtained taken from the peel-off layers further confirm their different microstructures. However, both show a quasi-amorphous feature, where the obtained selected area electron diffraction (SAED) pattern shows no distinct rings (Fig. 2f and g). The faintly visible diffraction rings can be indexed separately to quasi-amorphous NiFe alloy phase and FeOOH species for NiFe\_FA\_NN and nickel phosphide ( $\text{NiP}_2$ ) species for NiFeP\_FA\_NN. The scanning transmission electron microscopy (STEM) images and corresponding EDX mapping images (Fig. 2h and i) indicate the uniform distribution of elemental Ni, Fe, and O on NiFe\_FA\_NN nanoparticles, elemental Ni, Fe, and P uniformly distributing on nanoporous NiFeP\_FA\_NN, respectively.

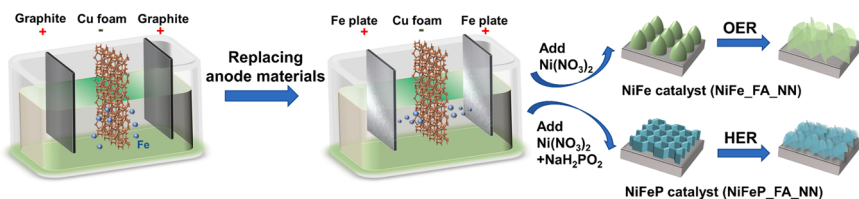


Fig. 1. Schematic of the synthesis process of NiFe\_FA\_NN and NiFeP\_FA\_NN in Ethaline-based DES, respectively.

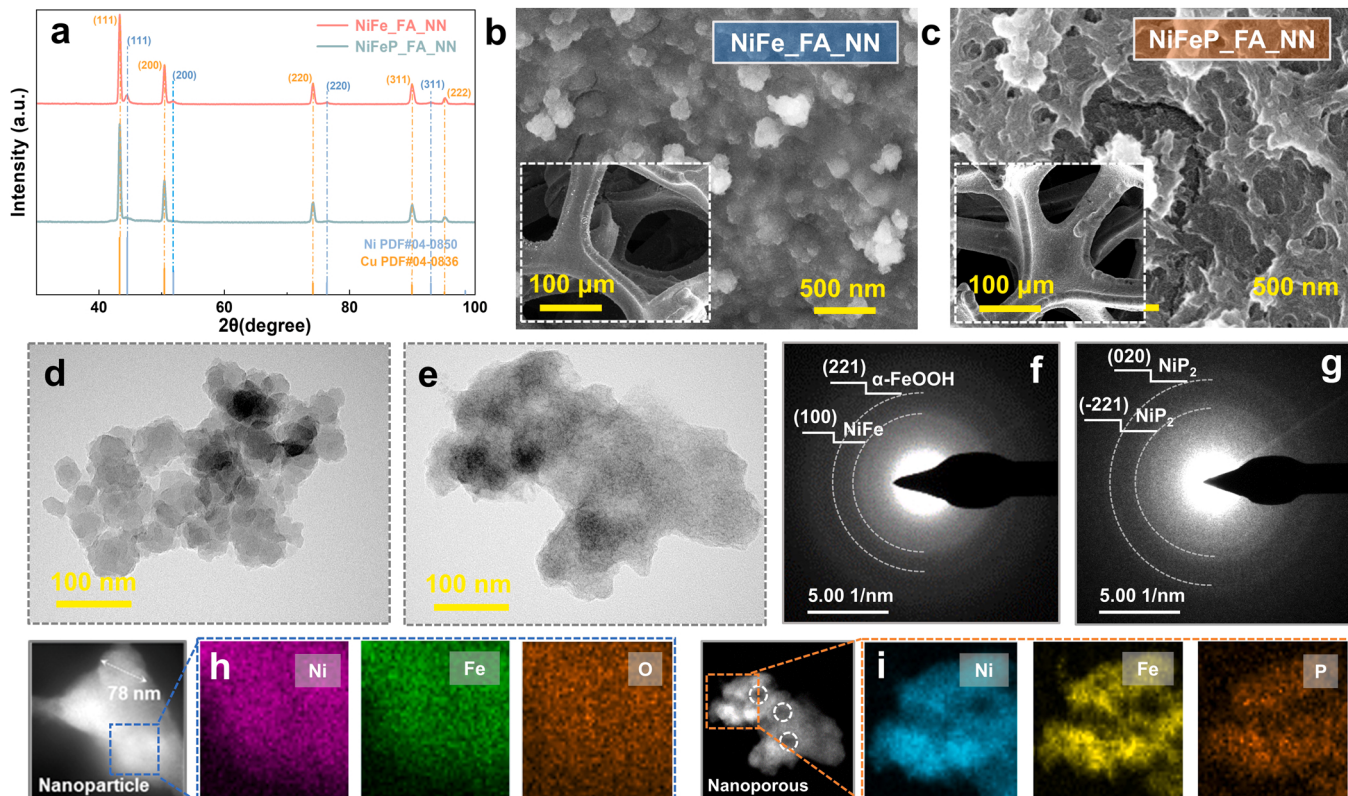
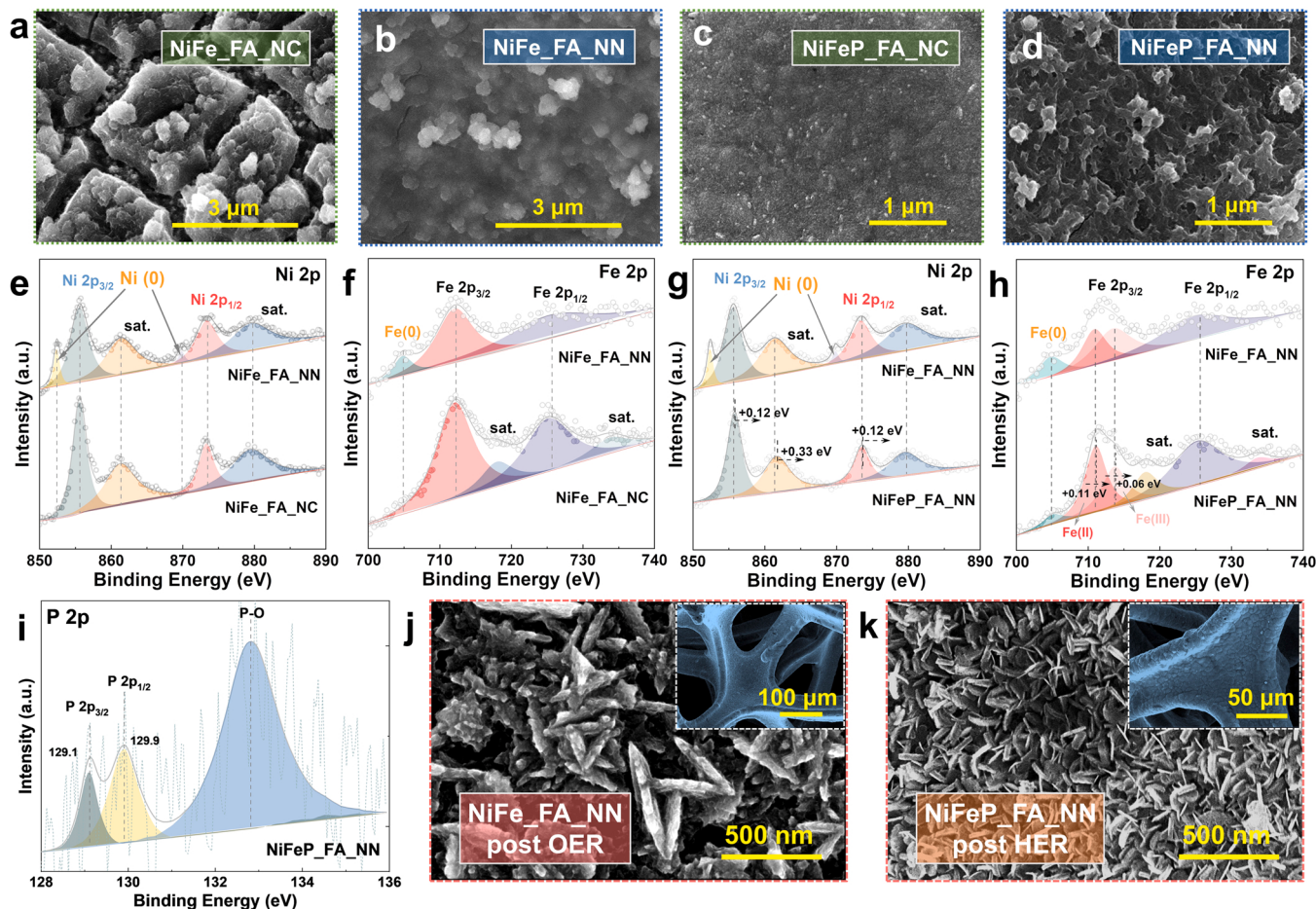


Fig. 2. (a) XRD patterns and SEM images of the as-prepared (b) NiFe\_FA\_NN and (c) NiFeP\_FA\_NN (insets show the low-magnification SEM images), respectively. TEM images of (d) NiFe\_FA\_NN and (e) NiFeP\_FA\_NN. Corresponding SAED patterns of (f) NiFe\_FA\_NN and (g) NiFeP\_FA\_NN. STEM images with EDX-mapping images of Ni, Fe, O elements in (h) NiFe\_FA\_NN and Ni, Fe, P elements in (i) NiFeP\_FA\_NN.

The influence of introduced anions on the electrodeposited NiFe-based electrodes was noticed. As can be seen from the SEM images, the cracked structure for NiFe\_FA\_NC (Fig. 3a) obtained with  $\text{NiCl}_2 \cdot 6\text{H}_2\text{O}$  as the Ni source is significantly different from the crack-free nanoparticle-packed structure for NiFe\_FA\_NN (Fig. 3b). A similar phenomenon occurs when P is doped. Compared with the smooth surface of NiFeP\_FA\_NC (Fig. 3c), NiFeP\_FA\_NN shows large porous networks (Fig. 3d), ensuring more active sites and ECSA for catalytic application. The formation of different morphologies is related to the differences in nucleation growth patterns and species formed during the electrodeposition process, which is affected by the different anions used [25]. Accordingly, some notable changes in the Ni and Fe XPS spectra are observed, as indicated by the investigation of the XPS. The comparison of the high-resolution Ni 2p spectra of NiFe\_FA\_NN and NiFe\_FA\_NC is shown in Fig. 3e. The binding energies of 852.4 eV and 869.9 eV correspond to metallic Ni on the surface [26], absent in the NiFe\_FA\_NC, indicating the different surface chemical states obtained by electrodeposition with two different anions. The two prominent peaks obtained at 855.6 eV (Ni 2p<sub>3/2</sub>) and 873.5 eV (Ni 2p<sub>1/2</sub>) for NiFe\_FA\_NN and NiFe\_FA\_NC can be indexed as  $\text{Ni(OH)}_2$ , together with two satellites peaks at 861.5 eV and 879.1 eV. The formation of surface  $\text{Ni(OH)}_2$  species is associated with the reaction of the Ni(II) ions and the in-situ

generated  $\text{OH}^-$  ions, which are formed through the electrochemical reduction of nitrate ions on the cathode [27]. The Fe 2p spectrum of NiFe\_FA\_NN (Fig. 3f) shows three main peaks, including a metallic Fe peak at 704.9 eV and two spin-orbit doublet peaks located at 712.3 eV and 726 eV, belonging to  $\text{FeOOH}$  [28]. In contrast, for NiFe\_FA\_NC, the binding energies of Fe 2p<sub>3/2</sub> (712.3 eV) and Fe 2p<sub>1/2</sub> (725.5 eV) with the satellites' peaks at 718.2 eV and 734.1 eV represent Fe oxidation states without metallic Fe on the surface. The surface of NiFe\_FA\_NN contains Ni and Fe in an elemental state in comparison to the NiFe\_FA\_NC, indicating the formation of an interfacial alloy. The local coordination environment offered by nitrate and DES is responsible for creating this hybrid structure with alloy and hydroxides.

After introducing P, the peak corresponding to metallic Ni disappears after P-doping, and the Ni 2p spectrum (Fig. 3g) positively shifts due to regulating the electronic structure around Ni by doping with P [29]. According to Fig. 3h, the Fe 2p<sub>3/2</sub> spectrum shows that the chemical state of Fe in the NiFeP\_FA\_NN surface tends to be mainly bivalent (711.1 eV), and the binding energies of divalent and trivalent Fe (713.8 eV) are positively shifted by 0.11 eV and 0.06 eV compared with the NiFe\_FA\_NN. This result suggests the presence of Fe-centered octahedra  $\text{FeP}_2$  species on the NiFeP\_FA\_NN surface in which Fe takes a valence state of 2+ [30]. The binding energy peak at around 713.7 eV



**Fig. 3.** Comparison of the SEM images of (a) NiFe\_FA\_NC, (b) NiFe\_FA\_NN, (c) NiFeP\_FA\_NC and (d) NiFeP\_FA\_NN. (e) Ni 2p and (f) Fe 2p XPS spectra of the NiFe\_FA\_NN and NiFe\_FA\_NC samples, respectively. (g) Ni 2p and (h) Fe 2p XPS spectra comparison of NiFe\_FA\_NN and NiFeP\_FA\_NN. (i) High-resolution P 2p spectrum of NiFeP\_FA\_NN. SEM images of (j) of NiFe\_FA\_NN post OER and (k) NiFeP\_FA\_NN post HER at  $10 \text{ mA m}^{-2}$  in  $1.0 \text{ M KOH}$  at  $25^\circ\text{C}$ , respectively.

corresponds to the surface oxidation of iron phosphides [30], which is confirmed by the P 2p spectrum (Fig. 3i), where two peaks for P  $2p_{3/2}$  and P  $2p_{1/2}$  at 129.1 eV and 129.9 eV are assigned to metal phosphides. The peak at 132.8 eV corresponding to the P-O group indicates the interfacial oxidation occurring on the surface [11]. The decrease in the peak intensity of the zero-valent metallic state caused by P doping indicates that the introduction of P tends to capture the outer electrons of Ni and Fe and generates shared electron pairs, causing the formation of higher valence states of metals. The electron transfer between P and Ni or Fe promotes the catalytic reaction process [31].

In addition to the differences in morphology and surface species caused by deposition with different Ni anions, evident structure changes are also observed for NiFe\_FA\_NN and NiFeP\_FA\_NN during the water-splitting process towards OER and HER, respectively, as shown in Fig. 3j and k. Both electrodes experience electrochemical-induced surface reconstruction after catalysis, resulting in two types of nanosheet-packed structures of different sizes.

### 3.2. Multi-vacancies induced by nitrate and electrochemical oxidation

For a deeper understanding of the structural evolution under catalysis and to outline the critical role of nitrate in the deposition process, detailed XPS, TEM, and Raman analyses on the samples before and after 24 h long-term OER operation ( $@10 \text{ mA m}^{-2}$  in  $1 \text{ M KOH}$  at  $25^\circ\text{C}$ ) were conducted. After the OER, XPS characterization reveals that the peaks of metallic Ni (Fig. 4a) and Fe (Fig. 4b) significantly decrease, suggesting the electrochemical leaching of Ni and Fe caused by the OER-driven in

situ oxidation. This leaching process can also be found in multi-step polarization measurement (Fig. S3a). The surface oxidation also leads to the proliferation of  $\text{Ni}^{3+}$  in the post-OER electrode (Fig. 4a). Combined with the ICP-OES results (Fig. S3b), the surface structural conversion process is accompanied by electrochemical leaching on the surface, which causes the formation of cation vacancies. A similar leaching manufacturing process for introducing Fe or Ni vacancies in the NiFe LDHs nanosheets has been previously discussed [32,33]. The lower Fe  $2p_{1/2}$  peak intensity and a negative shift of the binding energy (Fig. 4b) predicted more surface Fe vacancies created by electrochemical leaching during the OER process. For O 1s (Fig. 4c), a pronounced increase in the ratio of O<sub>2</sub> peak (low oxygen coordination of oxygen-vacancies) at 531.2 eV reveals that more oxygen-vacancies are formed in the post-OER-NiFe\_FA\_NN (Table 1). Our previous study [27] on different anions ( $\text{Cl}^-$  and  $\text{NO}_3^-$ ) effect on the deposited Ni-based catalysts in Ethaline-based DES revealed that the presence of  $\text{NO}_3^-$  ions led to the formation of defect-rich nickel hydroxide species on the surface of the Ni-based catalyst, which generated more oxygen vacancies after the OER process. The reconstructed surface with new proliferative multi-vacancies is usually considered the active site for OER [34,35].

The surface reconstruction of NiFe\_FA\_NN during the OER process is also revealed by high-resolution transmission electron microscopy (HRTEM), where the pristine disordered amorphous species (Fig. 4d) are converted to short-range ordered quasi-amorphous phases (Fig. 4e) after the OER process. The fast Fourier transform, and SAED images (inset of Fig. 4e) indicate that the surface phases of NiFe\_FA\_NN are mainly  $\gamma$ -NiOOH (PDF#06-0075) and quasi-amorphous FeOOH (PDF#22-

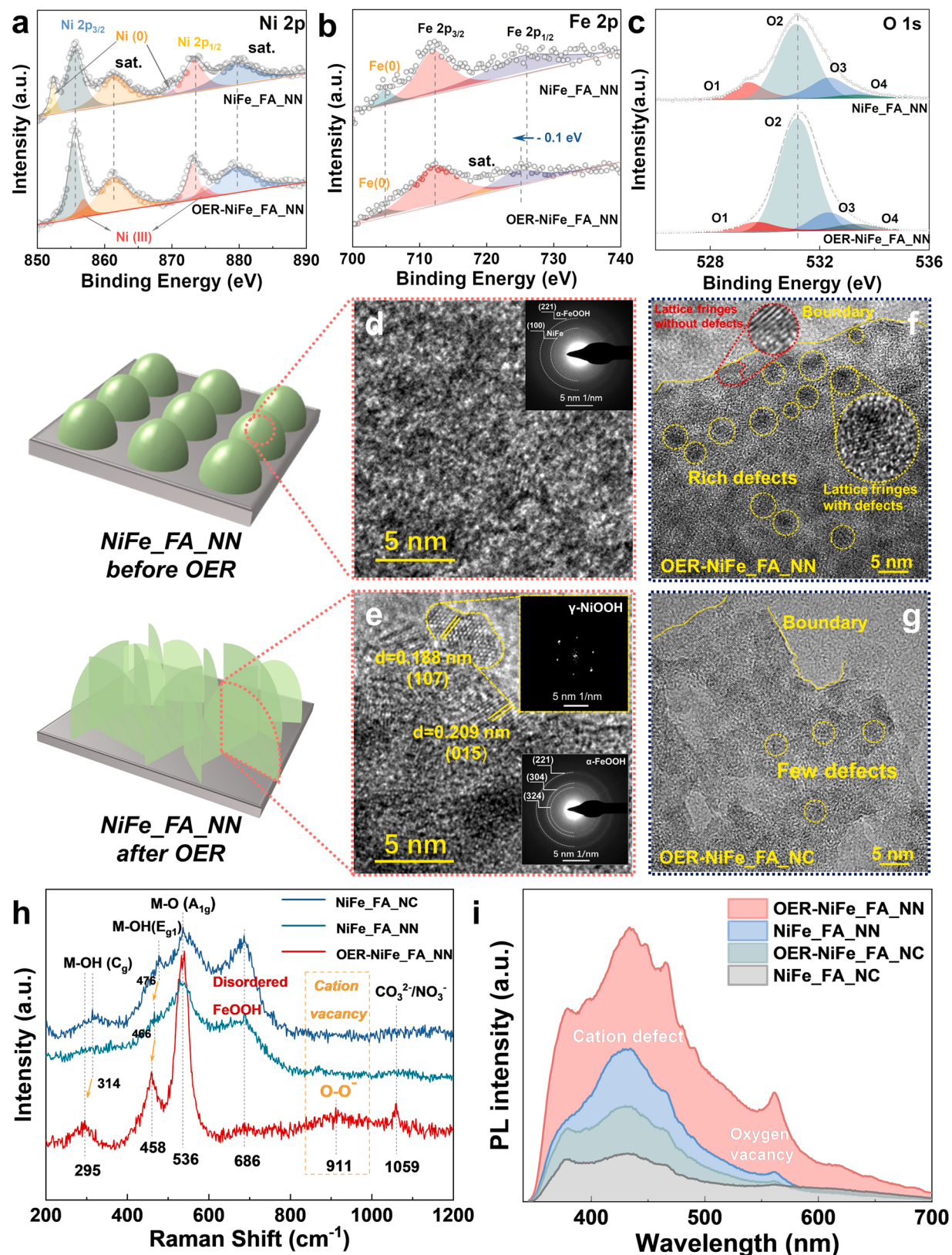


**Fig. 4.** Comparison of (a) Ni 2p, (b) Fe 2p, and (c) O 1 s XPS spectra of NiFe\_FA\_NN before and after OER. HRTEM images of NiFe\_FA\_NN (d) before and (e) after OER and (inset shows the SAED image and the local Fast Fourier Transform (FFT) image, respectively). HRTEM images of (f) NiFe\_FA\_NN and (g) NiFe\_FA\_NC after OER. (h) Raman spectra of NiFe\_FA\_NC and NiFe\_FA\_NN before and after OER. (i) The PL spectrum of NiFe\_FA\_NC and NiFe\_FA\_NN before and after OER.

**Table 1**

Comparison of the binding energy (eV) and the peak ratio of O 1 s before and after OER based on XPS analysis.

NiFe_FA_NN	O1 M-O (lattice oxygen)	O2 (oxygen vacancy)	O3 M-OH (hydroxide groups)	O4 M-H <sub>2</sub> O (chemical adsorbed water)
Initial	529.4 eV (21.6 %)	531.1 eV (36.6 %)	532.4 eV (23.3 )	533.4 eV (18.5 )
Post-OER	529.7 eV (8.5 %)	531.2 eV (85.7 %)	532.35 eV (5.2 )	533.4 eV (0.5 )

0353) [36]. In addition, the surface oxidation upon OER also brings about a defect-rich lattice structure observed by HRTEM (marked with yellow circles in Fig. 4f) [37], which is expected to enhance the electrocatalysis. In contrast, more lattice defects are formed for the post-OER-NiFe\_FA\_NN than for the post-OER-NiFe\_FA\_NC (Fig. 4g), caused by the differences in their initial surface states (Fig. 3e and f). It is also consistent with the results of XPS analysis (Fig. 4a and b) that the zero-valent Ni and Fe present on the surface of NiFe\_FA\_NN gradually dissolve in situ during the OER process, leading to a defect-rich surface. A similar law is also obtained for the NiFeP\_FA\_NN and NiFeP\_FA\_NC (Fig. S4). It turns out that the nitrate ions induced NiFe-based electrodes possess more active centers on the surface, favoring the formation of structural defects.

Furthermore, Raman spectroscopy analysis was employed to examine any surface changes caused by cation vacancies during the OER process. The Raman spectrum of the NiFe\_FA\_NC (Fig. 4h) shows three prominent characteristic bands at 476, 536, and 686 cm<sup>-1</sup>, assigned to the E<sub>g1</sub> bending mode of hydroxyl (M-OH) groups, the M-O A<sub>1g</sub> stretching mode, and the surface disordered FeOOH species, respectively [28,38]. In contrast, the characteristic peaks for the NiFe\_FA\_NN are comparatively weak, and the M-OH E<sub>g1</sub> bending mode is observed to negative shift to 466 cm<sup>-1</sup>. This phenomenon presumably occurs due to the lattice perturbation caused by the introduction of some surface defects [39]. Notably, the M-O (A<sub>1g</sub>) stretching mode of Ni<sup>II</sup>-O in defective or disordered Ni(OH)<sub>2</sub> significantly increases in the post-OER-NiFe\_FA\_NN [40]. Combined with TEM analysis (Fig. 4f), it can be inferred that more defects/cation vacancies are introduced in the post-OER-NiFe\_FA\_NN, resulting in negative Raman shifts of the hydroxyl (M-OH) groups (295 cm<sup>-1</sup> and 458 cm<sup>-1</sup>). The surface FeOOH species (686 cm<sup>-1</sup>) decline, suggesting a decrease in iron coordination number owing to the formation of Fe vacancies, consistent with the results of the Fe 2p XPS spectra (Fig. 4b). In addition, the Raman shift of post-OER-NiFe\_FA\_NN showed a faint vibration near 911 cm<sup>-1</sup>, similar to the NiOO<sup>-</sup> vibration (800–1200 cm<sup>-1</sup>) observed by the in-situ Raman analysis of the NiFe-LDH during the OER process [41]. It is suggested that the O<sup>2-</sup> in the solution can be captured by the cation vacancies during the OER and then combined with the lattice oxygen of the adjacent metal site to form O<sub>lat</sub>-O<sup>-</sup>, thus remaining the Raman signal of MOO<sup>-</sup> (M = Ni or Fe) intermediates. In this manner, the cation vacancy can excite the surrounding atoms as sites for the lattice oxygen mechanism (LOM), thus facilitating OER [42].

Crystal defects are closely related to the luminescence of material. Thus, PL spectroscopy was performed to confirm the presence of cation and anion vacancies on the electrode surface. According to Fig. 4i, the post-OER-NiFe\_FA\_NN showed obvious defect states, supported by an increase in the intensity of the emission peak at ~ 560 nm that is associated with the recombination of holes at the oxygen vacancies [43]. Additionally, a marked increase in emission peaks in the wide range of 380 ~ 490 nm after the OER suggests the proliferation of cation defects [44]. Defects introduced via nitrate also appear in similar reports [45]. Taken together, the NiFe\_FA\_NN surface after OER is rich in multi-vacancies, which are favorable for enhancing the OER kinetics.

XAFS spectroscopy was employed to accurately resolve local structural information to elucidate the coordination environment on the surface. Note that the system is rich in Ni ions at the initial deposition

stage. In contrast, Fe ions are slowly provided by anode dissolution. Such a deposition procedure leads to forming a thin layer of NiFe, dominant in Ni. The relatively low mass loading of Fe makes it difficult to obtain well-defined XAFS spectra. Therefore, Ni K-edge extended XAFS (EXAFS) spectra were used to analyze the local electronic structure of Ni in different NiFe samples [46,47]. As shown in the Fig. 5a, the XANES spectra for all prepared samples exhibit almost identical oscillations at the Ni K-edge compared to the Ni foil, indicating that the coordination environment in the average bulk phase of these samples matches with the Ni species of Ni foil. The obtained result can be interpreted as the deposition of metallic Ni in the underlying layer due to the lack of Fe in the early stages of electrodeposition. The bond lengths and coordination numbers (CNs) deriving from EXAFS curve fitting (Fig. S5) are displayed in Table S1. The Ni K-edge FT EXAFS (Fig. 5b) spectra for the NiFe\_FA\_NN and post-OER NiFe\_FA\_NN show a decrease in the Ni-M (M=Ni or Fe, ~2.17 Å) bond length compared with the typical Ni species in the reference Ni-foil, which supports the occurrence of the cation vacancies [40]. Compared with pure Ni-foil, the FT amplitude decreases with the addition of Fe, indicating that the ligand environment is distorted around the metal center (Fe and Ni), which has a positive effect on the promotion of OER activity [48]. In addition, the CNs of Ni-based bonds in the deposited samples are much lower than those for the Ni-foil, revealing that the lots of Ni atoms in these samples are coordinatively unsaturated. Affected by the discrepancy unsaturated coordination number of Ni in the deposited samples, the CNs of Ni-M in different NiFe samples exhibit little difference; however, the relatively low CNs obtained for the NiFe\_FA\_NN and post-OER-NiFe\_FA\_NN further demonstrate that more defects created [49], under the synergistic effect of nitrate-induced deposition and in-situ OER process. It is expected that the formation of abundant vacancies can be served as active sites to improve the OER performance significantly.

Based on the above demonstration, DFT calculations were conducted to further investigate the specific roles of different vacancies concerning the adsorption energy ( $\Delta G_{ae}$ ) of the reaction intermediates. Since the formation of active NiFe hydroxides on the NiFe\_FA\_NN surface after OER are confirmed by the HRTEM and Raman characterizations (Fig. 4e and h), the vacancy-rich post-OER NiFe\_FA\_NN can be modeled by pristine Ni(Fe)OOH and Ni(Fe)OOH with different vacancies, as shown in Fig. 5c, having a Ni/Fe ratio of 8:1, based on the stoichiometric ratio determined by ICP-OES measurements. OER intermediates were calculated based on NiOOH (001) surfaces with Ni and O vacancies (Fig. 5d and Fig. S6). Fig. 5e shows the multistep reaction energy barriers of the reaction performed on the Ni site of the calculated surface that is based on vacancy creation. Compared with the pristine Ni(Fe)OOH (gray), the surface with O vacancies (Ni(Fe)OOH(V<sub>O</sub>), red) exhibits intense adsorption energy of intermediates OH<sup>\*</sup> ( $\Delta G_{ae} = -1.64$  eV), O<sup>\*</sup> ( $\Delta G_{ae} = -1.97$  eV), and OOH<sup>\*</sup> ( $\Delta G_{ae} = -1.48$  eV). In contrast, the existence of Ni vacancies (Ni(Fe)OOH(V<sub>Ni</sub>), blue) suggests a huge stripping trend of the O<sup>\*</sup> ( $\Delta G_{ae} = +0.75$  eV) and OOH<sup>\*</sup> ( $\Delta G_{ae} = +1.86$  eV) species on the Ni site. Since strong adsorption or desorption is not conducive to the reactions, the coordinate regulation of the multi-vacancies consists of O<sup>2-</sup> and Ni<sup>2+</sup> (Ni(Fe)OOH(V<sub>O</sub>+V<sub>Ni</sub>), green) is supposed to optimize the adsorption or desorption of the intermediates on the Ni sites. As expected, the formation of the OOH<sup>\*</sup> intermediate, known as the determination step of OER [50], requires only  $\Delta G_{ae} = +0.3$  eV on the Ni(Fe)OOH(V<sub>O</sub>+V<sub>Ni</sub>). It turns out that the creation of multi-vacancies on the NiFe structure can optimize the binding energy of the intermediates during the OER process, thus consequently improving the catalytic activity.

### 3.3. OER electrocatalytic performance

The catalytic performance of as-synthesized NiFe\_FA\_NN, NiFe\_FA\_NC, and NiFe\_GA\_NN was evaluated in N<sub>2</sub>-saturated 1.0 M KOH, as displayed in Fig. 6a. As expected, NiFe\_FA\_NN exhibits higher catalytic activity than the other electrodes employed. The overpotential ( $\eta$ ) at

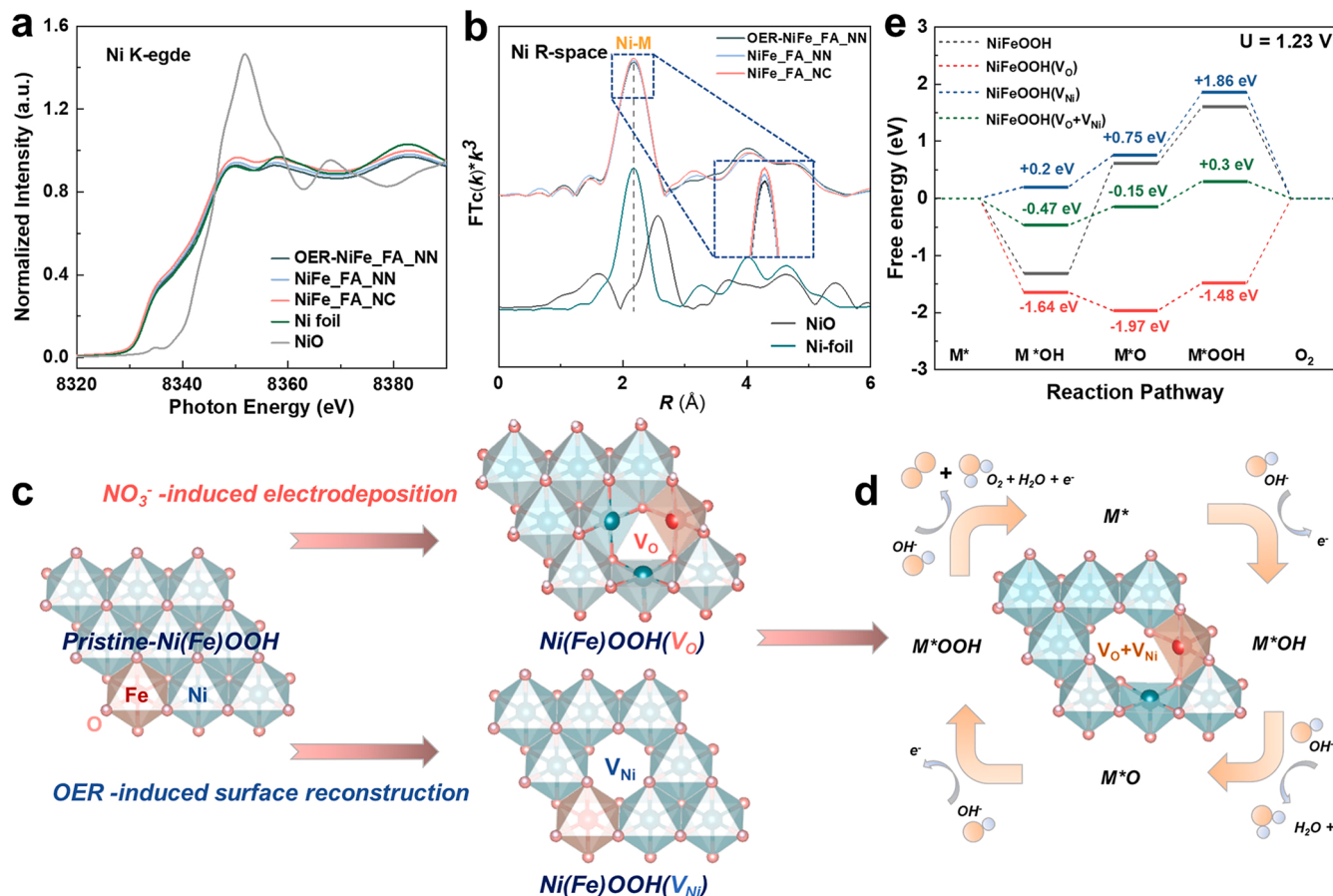


**Fig. 5.** (a) Ni K-edge XANES spectra of different samples in reference to Ni foil and NiO. (b) The corresponding  $k^3$  weighted Fourier-transformed EXAFS R-space patterns for Ni of different samples. (c) Crystal structures diagram of the pristine  $\text{Ni(Fe)OOH}$  and  $\text{Ni(Fe)OOH}$  with different vacancies. (d) OER mechanism on the  $\text{NiFeOOH}$  (001) surface. (e) Gibbs free energy profiles of  $\text{NiFeOOH}$  with different crystal structures along the OER reaction pathway.

10  $\text{mA cm}^{-2}$  for  $\text{NiFe}_\text{FA\_NN}$  ( $\eta_{10} = 256 \text{ mV}$ ) is much lower than that of  $\text{NiFe}_\text{GA\_NN}$  ( $\eta_{10} = 290 \text{ mV}$ ). In particular, the current increases rapidly with scanning potential for  $\text{NiFe}_\text{FA\_NN}$ , which shows superior catalytic activity at a high current density. Accordingly, the lowest Tafel slope obtained on  $\text{NiFe}_\text{FA\_NN}$  ( $56 \text{ mV dec}^{-1}$ ) compared to  $\text{NiFe}_\text{FA\_NC}$  ( $69 \text{ mV dec}^{-1}$ ) and  $\text{NiFe}_\text{GA\_NN}$  ( $91 \text{ mV dec}^{-1}$ ) indicates its favorable kinetics towards the OER process (Fig. 6b). Notably, even without iR-compensation, the catalytic performance of our  $\text{NiFe}_\text{FA\_NN}$  is comparable to the previously reported  $\text{NiFe}$ -based robust OER electrocatalysts (Fig. 6c). A more comprehensive comparison is presented in Table S2. EIS was further performed to investigate the electron and charge transfer performance of the developed electrodes. The associated Nyquist plots obtained at 1.51 V vs. RHE are compared in Fig. 6d with an equivalent circuit model inserted. The low-frequency response is attributed to the charge transfer resistance  $R_{\text{ct}}$ , and the high-frequency response is correspondingly assigned to the solution resistor  $R_S$  and resistance  $R_1$ , which is the resistance associated to charge diffusion in the space charge layer [51].  $\text{NiFe}_\text{FA\_NN}$  ( $1.74 \Omega$ ) exhibits a significantly reduced  $R_{\text{ct}}$  as compared to  $\text{NiFe}_\text{FA\_NC}$  ( $2.77 \Omega$ ) and  $\text{NiFe}_\text{GA\_NN}$  ( $4.47 \Omega$ ), revealing the enhanced charge transfer efficiency and favorable reaction kinetics on the vacancy-rich  $\text{NiFe}$  electrode.

To further understand the enhancement of OER activity, the mass activity of prepared  $\text{NiFe}_\text{FA\_NN}$  (mass loading:  $4.3 \text{ mg cm}^{-2}$ ),  $\text{NiFe}_\text{FA\_NC}$  ( $5.3 \text{ mg cm}^{-2}$ ), and  $\text{NiFe}_\text{GA\_NN}$  ( $8.8 \text{ mg cm}^{-2}$ ) at 1.6 V vs. RHE were compared (Fig. 6e). The  $\text{NiFe}_\text{FA\_NN}$  possesses a mass activity of  $16.92 \text{ A g}^{-1}$  at the potential of 1.6 V, much higher than  $\text{NiFe}_\text{FA\_NC}$  ( $12.19 \text{ A g}^{-1}$ ) and  $\text{NiFe}_\text{GA\_NN}$  ( $4.67 \text{ A g}^{-1}$ ). In addition, the ECSA of the as-deposited  $\text{NiFe}$  electrodes was estimated from the non-Faradaic electrochemical  $C_{\text{dl}}$  via a CV method scanning at different scan rates

(Figs. S7 a-c). The mass loading-ECSA corrected specific activity was further calculated to investigate their intrinsic activity (Fig. 6e and Fig. S8a). Based on the  $C_{\text{dl}}$  value (Fig. S8b), the calculated specific activity of  $\text{NiFe}_\text{FA\_NN}$  is  $0.186 \text{ A g}^{-1} \text{ cm}_{\text{ECSA}}^{-2}$ , 3.1 and 4.5 times higher than that of  $\text{NiFe}_\text{GA\_NN}$  ( $0.06 \text{ A g}^{-1} \text{ cm}_{\text{ECSA}}^{-2}$ ) and  $\text{NiFe}_\text{FA\_NC}$  ( $0.041 \text{ A g}^{-1} \text{ cm}_{\text{ECSA}}^{-2}$ ). Such a high intrinsic activity of the  $\text{NiFe}_\text{FA\_NN}$  should be associated with the unique evolved multi-vacancies features during the OER, which results in the regulation of the electronic environment of the active sites and boosts the OER activity. Moreover, multiple CV scans and multi-step chronopotentiometry testing were used to examine the endurance and robustness of the  $\text{NiFe}_\text{FA\_NN}$ . Stability experiments were first performed in 1.0 M KOH using repeated cycle CV measurements with potentials ranging from 1.20 to 1.80 V vs. RHE at a scan rate of  $100 \text{ mV s}^{-1}$ . The  $\text{NiFe}_\text{FA\_NN}$  exhibits good stability, as demonstrated in Fig. 6f, with a low activity decline after 4000 continuous potential sweeps. The evolved nanosheets are still uniformly covered on the surface with slight aggregation after successive CV cycles (Fig. S9a). Impressively, the  $\text{NiFe}_\text{FA\_NN}$  catalyst also exhibits outstanding stability under different current densities ranging from 10 to 500  $\text{mA cm}^{-2}$  during a multi-current process (inset of Fig. 6f), demonstrating its robust structural features that can adapt to higher current density and continuous current change.

### 3.4. HER electrocatalytic performance

Similar to previous studies, the HER performance of  $\text{NiFe}$ -based OER catalysts can be significantly improved by introducing P via our proposed electrodeposition approach (Fig. S10). The HER activity of the as-deposited  $\text{NiFeP}$  electrodes was evaluated by measuring the polarization

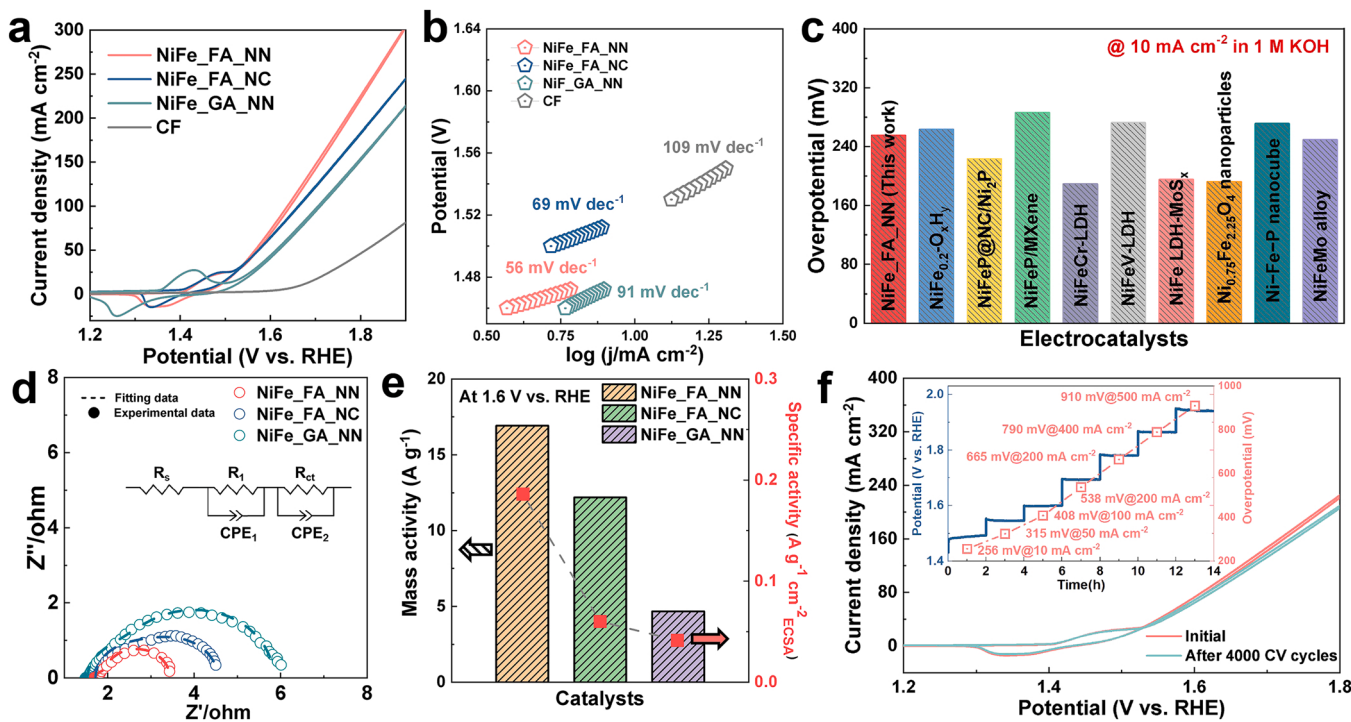


**Fig. 6.** (a) Polarization curves of as-deposited NiFe catalysts with different set-ups and nickel salts performed in 1.0 M KOH. (b) The corresponding Tafel plots. (c) Comparison of our catalyst with the previously reported NiFe-based OER catalysts. (d) Nyquist plots of different catalysts obtained at 1.51 V vs. RHE. Inset is the equivalent circuit model for EIS data fitting. (e) Comparison of mass activity and mass loading-ECSA corrected specific activity of NiFe\_FA\_NN, NiFe\_FA\_NC, and NiFe\_GA\_NN at 1.6 V vs. RHE. (f) Polarization curves of NiFe\_FA\_NN before and after successive 4000 CV cycles (The data are obtained without iR-correction). Inset is the multi-current process for NiFe\_FA\_NN in 1.0 M KOH.

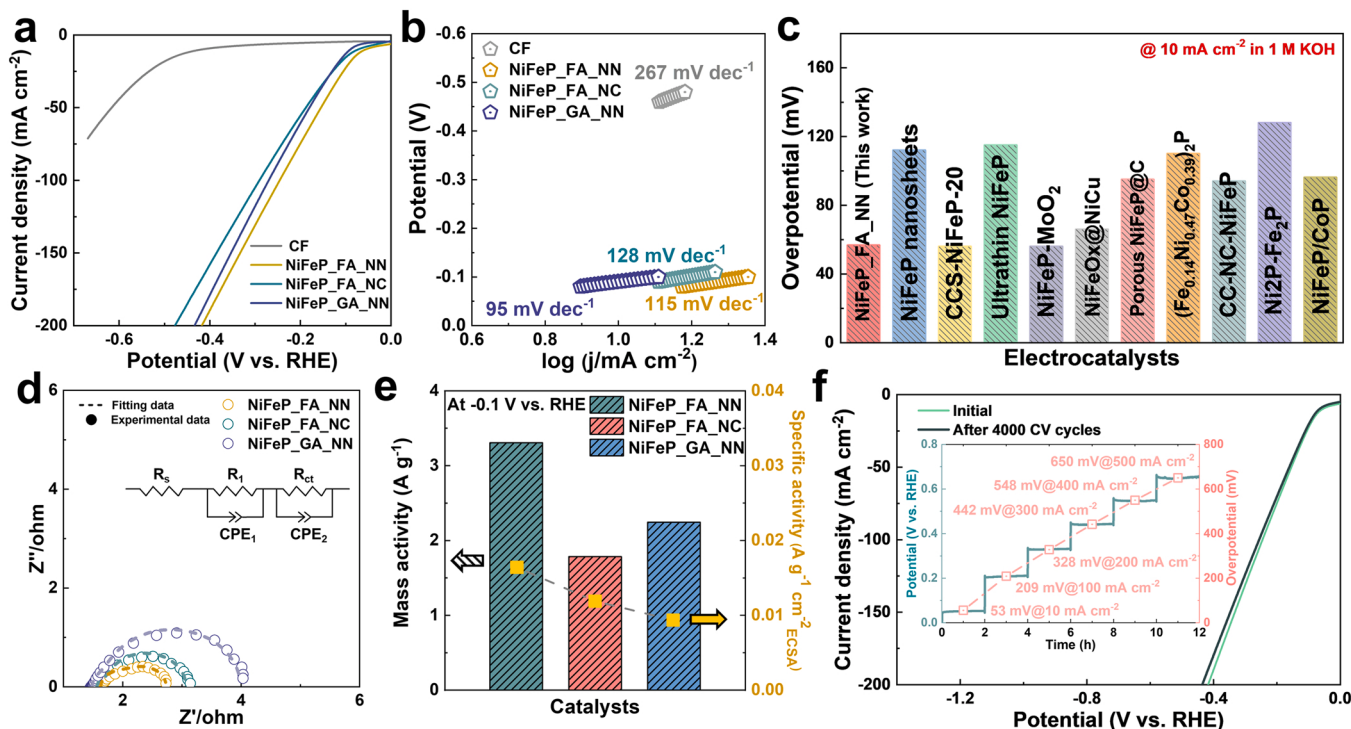


**Fig. 7.** (a) Polarization curves of as-deposited NiFeP catalysts with different set-ups and nickel salts performed in 1.0 M KOH. (b) The corresponding Tafel plots. (c) Comparison of our catalyst with the previously reported NiFeP-based HER catalysts. (d) Nyquist plots of different NiFeP catalysts obtained at a potential of -102 mV vs. RHE. (e) Comparison of the mass activity and mass loading-ECSA corrected specific activity of NiFeP\_FA\_NN, NiFeP\_GA\_NN, and NiFeP\_FA\_NC at -0.1 V vs. RHE. (f) LSV curves of NiFeP\_FA\_NN before and after successive 4000 CV cycles (The data are obtained without iR-correction). Inset is the multi-current process for NiFeP\_FA\_NN in 1.0 M KOH.

curves without iR-compensation in  $N_2$ -saturated 1.0 M KOH, as shown in Fig. 7a. In a direct comparison, NiFeP\_FA\_NN shows superior HER catalytic performance, driving 10  $mA\ cm^{-2}$  with an overpotential of 56 mV ( $\eta_{10} = 56$  mV), which is much lower than NiFeP\_GA\_NN ( $\eta_{10} = 74$  mV) and NiFeP\_FA\_NC ( $\eta_{10} = 90$  mV). Although the Tafel slope of NiFeP\_FA\_NN is not at the upper level (Fig. 7b), the low overpotential required is found to compare favorably to some NiFeP-based HER electrocatalysts recently reported (Fig. 7c and Table S3). Accordingly, NiFeP\_FA\_NN shows the lowest  $R_{ct}$  (1.1  $\Omega$ ) among the three NiFeP catalysts (1.48  $\Omega$  for NiFeP\_FA\_NC and 2.47  $\Omega$  for NiFeP\_GA\_NN) at a given potential of  $-102$  mV vs. RHE (Fig. 7d), indicating a faster charge transfer ability during the HER. These features demonstrate that the enhanced reaction kinetics of our developed NiFeP samples obtained via the nitrate ion-induced electrodeposition strategy facilitate the HER catalytic process. Furthermore, the mass activity and mass loading-ECSA corrected specific activity of the as-deposited NiFeP electrodes were also estimated, as shown in Fig. 7e and Fig. S8c. The corresponding  $C_{dl}$  values are depicted in Fig. S8d. With the highest mass activity ( $3.3\ A\ g^{-1}$  at  $-0.1$  V) among the prepared NiFeP-based catalysts (NiFeP\_FA\_NC:  $1.785\ A\ g^{-1}$ ; NiFeP\_GA\_NN:  $2.24\ A\ g^{-1}$ ), the NiFeP\_FA\_NN also displays a high intrinsic activity of  $0.0164\ A\ g^{-1}\ cm^{-2}\text{ECSA}$ , which is higher than

that of NiFeP\_GA\_NN ( $0.012\ A\ g^{-1}\ cm^{-2}\text{ECSA}$ ) and NiFeP\_FA\_NC ( $0.0093\ A\ g^{-1}\ cm^{-2}\text{ECSA}$ ). The improved catalytic activity of NiFeP\_FA\_NN should be related to the regulated electronic structure of active sites by P doping [52], which increases the intrinsic activity of active sites and favors fast charge transfer. Such an integrated structure with porous architecture endows the NiFeP\_FA\_NN with excellent catalytic stability, allowing it to maintain good performance after 4000 successive cycle CV measurements (Fig. 7f) and function well during a multi-current process, especially at high current conditions (inset of Fig. 7f). The well-defined nanosheet features of the post-HER electrode remains essentially unchanged (Fig. S9b), confirming its structural stability.

### 3.5. Practical performance in simulated industrial conditions

For large-scale hydrogen production, industrial water electrolysis needs to be carried out at high temperatures and electrolyte concentrations. The performance of industrial catalysts also should be evaluated under practical working conditions. However, most performance data reported in the literature are iR-compensated, where R is usually identified as the solution resistance. Obviously, this type of resistance is unavoidable in an actual electrolyzer, meaning that this portion of

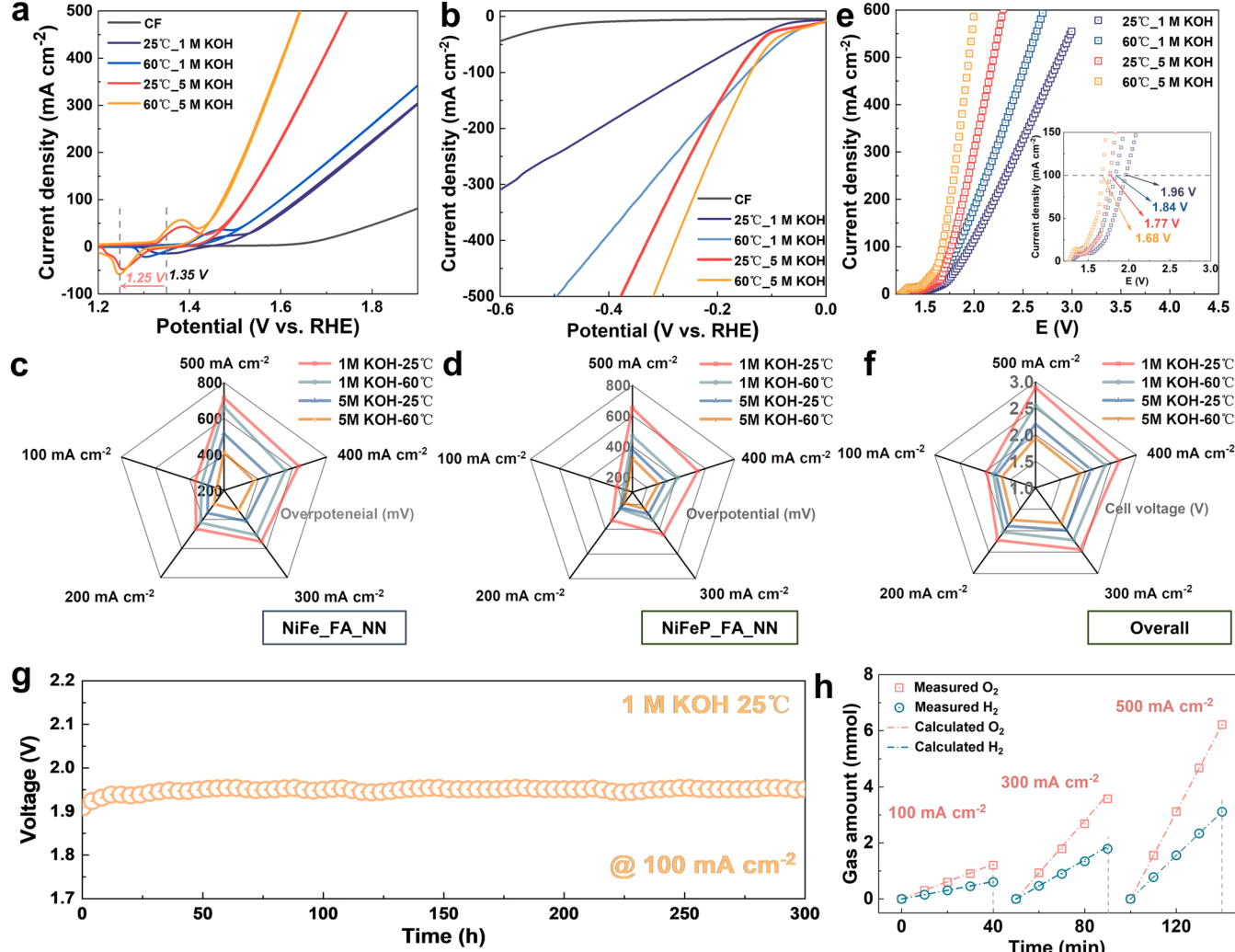


**Fig. 8.** CV curves of (a) NiFe\_FA\_NN and polarization curves of (b) NiFeP\_FA\_NN for the OER and HER, respectively, performed in 1.0 and 5.0 M KOH at 25 °C and 60 °C (as indicated). Overpotentials required for (c) NiFe\_FA\_NN and (d) NiFeP\_FA\_NN obtained under different conditions. (e) Polarization curves of the overall water splitting with NiFe\_FA\_NN<sup>(+)</sup>||NiFeP\_FA\_NN<sup>(-)</sup>. (f) Summary of the overall water splitting cell voltage required for NiFe\_FA\_NN<sup>(+)</sup>||NiFeP\_FA\_NN<sup>(-)</sup> obtained at different conditions. (g) Durability measurement of self-assembling two-electrode water splitting electrolyzer with NiFe\_FA\_NN<sup>(+)</sup>||NiFeP\_FA\_NN<sup>(-)</sup> at 100  $mA\ cm^{-2}$  in 1.0 M KOH at 25 °C for 300 h. (h)  $H_2$  and  $O_2$  amount for NiFe\_FA\_NN<sup>(+)</sup>||NiFeP\_FA\_NN<sup>(-)</sup> collected at different current densities in 1.0 M KOH at 25 °C.

energy consumption must be taken into account for evaluating the practical performance, especially under industrial conditions [53]. As shown in Fig. S11, Table S4, and Table S5, compensation for the overpotential at a high current density can lead to misjudgment of the actual catalytic performance for the measured catalyst. Therefore, the electrochemical data presented in this work is not iR-compensated.

The CV curves clearly show the effects of temperature (25 °C and 60 °C) and electrolyte concentration (1.0 and 5.0 M KOH) on the electrochemical redox behavior of the NiFe\_FA\_NN electrode during the OER process (Fig. 8a). An apparent peak shift can be found in the curves at a high electrolyte concentration, while a higher temperature significantly enhances the redox peak. Cathodic peaks located at 1.25 and 1.35 V are observed in the CVs of NiFe\_FA\_NN under different conditions, which should be assigned to the reduction of  $\beta(\gamma)\text{-}(NiFe)OOH \rightarrow Ni_xFe_y(OH)_2$ , respectively [38]. These changes can be interpreted as the crystal structure and phase transformation between  $Ni(OH)_2$  and  $NiOOH$  caused by aging and overcharging in a high pH environment [54]. Increases in temperature and electrolyte concentration promote the interfacial phase transformation of  $Ni(OH)_2 \rightarrow NiOOH$  via an in-situ electrochemical oxidation process [54], resulting in significantly improved catalytic activity. Similarly, the HER performance of NiFeP\_FA\_NN increases obviously with increasing temperature and electrolyte concentration (Fig. 8b). The overpotentials required for NiFe\_FA\_NN (Fig. 8c) and NiFeP\_FA\_NN (Fig. 8d) obtained at different conditions toward OER and HER, respectively, are compared. Noted that both NiFe\_FA\_NN and NiFeP\_FA\_NN showed no oscillations or fluctuations in their curves at high current density, even at high temperature and high concentration, revealing that both catalysts have remarkable electrolyte wettability structure and favorable bubble overflow kinetics.

Encouraged by the excellent catalytic performance of NiFe\_FA\_NN and NiFeP\_FA\_NN for the OER and HER, respectively, a two-electrode alkaline water electrolyzer was assembled with NiFe\_FA\_NN as the anode and NiFeP\_FA\_NN as the cathode (denoted as  $NiFe_FA_NN^{(+)} \parallel NiFeP_FA_NN^{(-)}$ ) to explore its overall water splitting performance. Fig. 8e shows the polarization curves of overall water splitting at different conditions with the  $NiFe_FA_NN^{(+)} \parallel NiFeP_FA_NN^{(-)}$ , in which the cell voltage obtained at

different current densities (shown in Fig. 8f) is in good correspondence with the sum of overpotentials required for the single catalyst. Fig. 8g shows the durability test of NiFe\_FA\_NN and NiFeP\_FA\_NN electrodes combined in self-assembling two-electrode water splitting electrolyzer. The electrolyzer achieves a high current density of  $100 \text{ mA cm}^{-2}$  at a cell voltage of 1.96 V in 1 M KOH at room temperature and functions stably for 300 h. A built H-type electrolytic cell (Fig. S12) is used to gather hydrogen and oxygen gases generated during the water electrolysis process. Compared with the calculated theoretical gas product amount, the self-assembling electrolyzer can maintain a good water electrolysis efficiency (97–99 %) at different current densities (Fig. 8h).

To further explore the practicability of the prepared catalysts, the overall water splitting performance was evaluated by a homemade AEM electrolyzer loaded with  $NiFe_FA_NN^{(+)} \parallel NiFeP_FA_NN^{(-)}$ , as displayed in Fig. 9a. To meet the scale of industrial production, amplification experiments were carried out to prepare catalysts with larger area sizes ( $3.2 \times 3.2 \text{ cm}^2$  and  $5 \times 5 \text{ cm}^2$ ) for the AEM electrolyzer (Fig. S13). Notably, our NiFe\_FA\_NN and NiFeP\_FA\_NN can be electrodeposited on various conductive substrates such as Cu foam, Ni foam, and Fe foam with flexible sizes (Fig. S14), suggesting the scalability of the proposed electrodeposition approach. Fig. 9b and Fig. S15 show the disassembly diagram and optical images of the homemade AEM water electrolysis device. The catalysts loaded on a foam substrate are sealed to both sides of the low internal resistance anion exchange membrane (FAA-3-PE-30) with bipolar plates and fluorine rubber gaskets. The current-voltage curves obtained using the AEM device under different electrolysis conditions are shown in Fig. 9c. As expected, the device exhibits excellent water splitting performance, especially in 5 M KOH at 60 °C, demonstrating the high activity of our catalysts under harsh industrial conditions. The AEM electrolyzer with  $NiFe_FA_NN^{(+)} \parallel NiFeP_FA_NN^{(-)}$  exhibits exceptional stability at  $10 \text{ and } 500 \text{ mA cm}^{-2}$  for 200 h and requires low cell voltages of 1.51 V and 2.14 V in 1.0 M KOH at 60 °C with an effective area of  $10 \text{ cm}^2$  (Fig. 9d). Impressively, the AEM electrolyzer can also operate stably at an industrial-grade current density of  $1000 \text{ mA cm}^{-2}$  with a competitive output cell voltage of 1.73 V for 200 h (Fig. 9e) under simulated industrial conditions of 5.0 M KOH at 60 °C. From the macro picture (Figs. S16 a-b), the fabricated

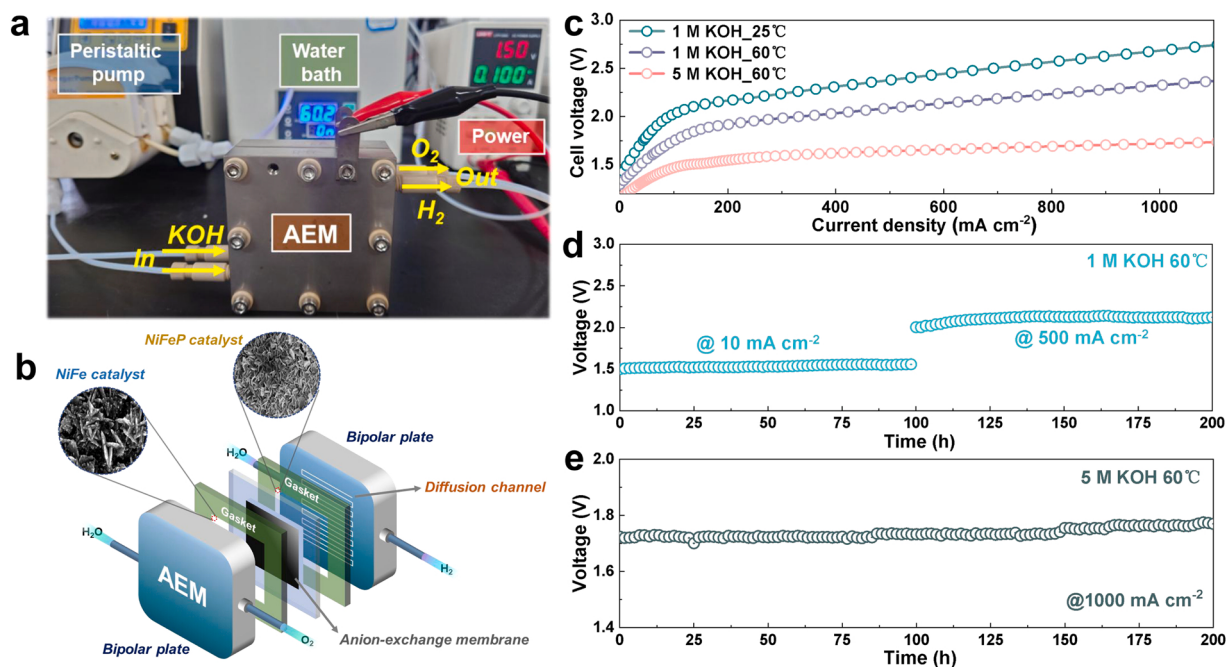


Fig. 9. (a) Photograph of a homemade AEM electrolyzer loaded with  $NiFe_FA_NN^{(+)} \parallel NiFeP_FA_NN^{(-)}$  performed in 1.0 M KOH at 60 °C. (b) Schematic of the AEM electrolyzer internal structure dismantling. (c) Current–voltage curves of AEMWE operated at different conditions. (d–e) Durability measurements of the AEM electrolyzer with  $NiFe_FA_NN^{(+)} \parallel NiFeP_FA_NN^{(-)}$  in 1.0 M KOH at 60 °C and 5.0 M KOH at 60 °C.

NiFeP\_FA\_NN and NiFe\_FA\_NN show negligible corrosive dissolution or disintegration after long-term water electrolysis for 200 h under such a quasi-industrial condition, illustrating the tremendous bonding force of the active coatings on the substrate and extremely robust stability. The corresponding SEM images further verify their stable microstructure (Fig. S16 c-f). The outstanding stability and activity of our catalysts compare favorably to most previously reported nonprecious metal-based electrocatalysts that were used in the AEM cells (Table S6). These results indicate their promising prospect toward practical water electrolysis on an industrial scale. As the application of the AEM electrolyzer is limited by the performance and life of the anion exchange membrane, the exploration can be further optimized by developing and replacing better anion exchange membranes.

#### 4. Conclusion

In summary, we have reported a general electrodeposition synthesis approach with an updated sacrificial anode set-up from Ethaline-based DES to fabricate high-performance NiFe-based catalysts for overall water splitting. It is interesting to discover that the introduction of nitrate can induce the formation of NiFe-based electrodes with more structural defects, which favors the generation of multi-vacancies by the OER-driven electrochemical leaching. The synergistic effect of the proliferative multi-vacancies on the deposited NiFe structures regulates the active sites and adsorption energy to boost the OER. P doping into the NiFe catalyst leads to a porous network structure with the tailored electronic structure, which endows the electrode with significantly enhanced HER catalytic performance. AEM electrolyzer loaded the pair of NiFe\_FA\_NN<sup>(+)</sup>||NiFeP\_FA\_NN<sup>(-)</sup> shows excellent overall water splitting catalytic performance (1.73 V<sub>cell</sub>) and works stability (200 h) under simulated industrial conditions at 1000 mA cm<sup>-2</sup> in 5.0 M KOH + 60 °C. Our work provides a simple and scalable method for preparing high-performance NiFe-based catalysts, promising for industrial water electrolysis.

#### CRediT authorship contribution statement

**Zhuoming Wei:** Writing – original draft, Data, Methodology, Investigation, Visualization, Data curation. **Mengwei Guo:** Writing – review & editing. **Qibo Zhang:** Project administration, Funding acquisition, Supervision, Resources, Conceptualization, Writing – review & editing.

#### Declaration of Competing Interest

The authors declare that they have no known competing financial interests or personal relationships that could have appeared to influence the work reported in this paper.

#### Data availability

Data will be made available on request.

#### Acknowledgements

The authors gratefully acknowledge the financial support of the National Natural Science Foundation of China (21962008), Yunnan Province Excellent Youth Fund Project (202001AW070005), Candidate Talents Training Fund of Yunnan Province (2018HB007), and Yunnan Ten Thousand Talents Plan Young & Elite Talents Project (YNWR-QNBJ-2018-346).

#### Appendix A. Supporting information

Supplementary data associated with this article can be found in the online version at [doi:10.1016/j.apcatb.2022.122101](https://doi.org/10.1016/j.apcatb.2022.122101).

#### References

- [1] J. Xu, I. Amorim, Y. Li, J. Li, Z. Yu, B. Zhang, A. Araujo, N. Zhang, L. Liu, Stable overall water splitting in an asymmetric acid/alkaline electrolyzer comprising a bipolar membrane sandwiched by bifunctional cobalt-nickel phosphide nanowire electrodes, *Carbon Energy* 2 (2020) 646–655, <https://doi.org/10.1002/cey.256>.
- [2] Q. Che, Q. Li, Y. Tan, X. Chen, X. Xu, Y. Chen, One-step controllable synthesis of amorphous (Ni-Fe)S /NiFe(OH) hollow microtube/sphere films as superior bifunctional electrocatalysts for quasi-industrial water splitting at large-current-density, *Appl. Catal. B* 246 (2019) 337–348, <https://doi.org/10.1016/j.apcatb.2019.01.082>.
- [3] C.-T. Hsieh, C.-L. Huang, Y.-A. Chen, S.-Y. Lu, NiFeMo alloy inverse-opals on Ni foam as outstanding bifunctional catalysts for electrolytic water splitting of ultralow cell voltages at high current densities, *Appl. Catal. B* 267 (2020) 118376–118385, <https://doi.org/10.1016/j.apcatb.2019.118376>.
- [4] Y. Yang, F. Duan, B. Yi, M. Hou, Z. Shao, H. Yu, Hydrogen production by water electrolysis: progress and suggestions, *Chin. J. Eng. Sci.* 23 (2021) 146–152, <https://doi.org/10.15302/j-sscae-2021.02.020>.
- [5] J. Chi, H. Yu, Water electrolysis based on renewable energy for hydrogen production, *Chin. J. Catal.* 39 (2018) 390–394, [https://doi.org/10.1016/s1872-2067\(17\)62949-8](https://doi.org/10.1016/s1872-2067(17)62949-8).
- [6] K. Ayers, N. Danilovic, R. Quimet, M. Carmo, B. Pivovar, M. Bornstein, Perspectives on low-temperature electrolysis and potential for renewable hydrogen at scale, *Annu. Rev. Chem. Biomol. Eng.* 10 (2019) 219–239, <https://doi.org/10.1146/annurev-chembiogeo-060718-030241>.
- [7] J. Lee, H. Jung, Y.S. Park, N. Kwon, S. Woo, N.C.S. Selvam, G.S. Han, H.S. Jung, P. J. Yoo, S.M. Choi, J.W. Han, B. Lim, Chemical transformation approach for high-performance ternary NiFeCo metal compound-based water splitting electrodes, *Appl. Catal. B* 294 (2021) 120246–120255, <https://doi.org/10.1016/j.apcatb.2021.120246>.
- [8] W.Z. Zhang, G.Y. Chen, J. Zhao, J.C. Liang, L.F. Sun, G.F. Liu, B.W. Ji, X.Y. Yan, J. R. Zhang, Self-growth Ni<sub>2</sub>P nanosheet arrays with cationic vacancy defects as a highly efficient bifunctional electrocatalyst for overall water splitting, *J. Colloid Interface Sci.* 561 (2020) 638–646, <https://doi.org/10.1016/j.jcis.2019.11.039>.
- [9] X. Liu, R. Guo, K. Ni, F. Xia, C. Niu, B. Wen, J. Meng, P. Wu, J. Wu, X. Wu, L. Mai, Reconstruction-determined alkaline water electrolysis at industrial temperatures, *Adv. Mater.* 32 (2020), e2001136, <https://doi.org/10.1002/adma.202001136>.
- [10] Z. Pu, T. Liu, I.S. Amini, R. Cheng, P. Wang, C. Zhang, P. Ji, W. Hu, J. Liu, S. Mu, Transition-metal phosphides: activity origin, energy-related electrocatalysis applications, and synthetic strategies, *Adv. Funct. Mater.* 30 (2020), <https://doi.org/10.1002/adfm.202004009>.
- [11] Q. Quan, Z. Lai, Y. Bao, X. Bu, Y. Meng, W. Wang, T. Takahashi, T. Hosomi, K. Nagashima, T. Yanagida, C. Liu, J. Lu, J.C. Ho, Self-anti-stacking 2D metal phosphide loop-sheet heterostructures by edge-topological regulation for highly efficient water oxidation, *Small* 17 (2021), e2006860, <https://doi.org/10.1002/smll.202006860>.
- [12] Z. Kuang, S. Liu, X. Li, M. Wang, X. Ren, J. Ding, R. Ge, W. Zhou, A.I. Rykov, M. T. Sougrati, P.-E. Lippens, Y. Huang, J. Wang, Topotactically constructed nickel–iron (oxy)hydroxide with abundant in-situ produced high-valent iron species for efficient water oxidation, *J. Energy Chem.* 57 (2021) 212–218, <https://doi.org/10.1016/j.jec.2020.09.014>.
- [13] V. Maruthapandian, A. Muthurasi, A. Dekshinamoothi, R. Aswathy, S. Vijayaraghavan, S. Muralidharan, V. Saraswathy, Electrochemical cathodic treatment of mild steel as a host for Ni(OH)<sub>2</sub> catalyst for oxygen evolution reaction in alkaline media, *ChemElectroChem* 6 (2019) 4391–4401, <https://doi.org/10.1002/celec.201900655>.
- [14] C.T. Hsieh, X.F. Chuah, C.L. Huang, H.W. Lin, Y.A. Chen, S.Y. Lu, NiFe/(Ni, Fe)S<sub>2</sub> core/shell nanowire arrays as outstanding catalysts for electrolytic water splitting at high current densities, *Small Methods* 3 (2019) 1900234–1900242, <https://doi.org/10.1002/smtd.201900234>.
- [15] C. Xuan, J. Wang, W. Xia, Z. Peng, Z. Wu, W. Lei, K. Xia, H.L. Xin, D. Wang, Porous structured Ni-Fe-P nanocubes derived from a Prussian Blue analogue as an electrocatalyst for efficient overall water splitting, *ACS Appl. Mater. Interfaces* 9 (2017) 26134–26142, <https://doi.org/10.1021/acsami.7b08560>.
- [16] C. Yang, T. He, W. Zhou, R. Deng, Q. Zhang, Iron-tuned 3D cobalt–phosphate catalysts for efficient hydrogen and oxygen evolution reactions over a wide pH range, *ACS Sustain. Chem. Eng.* 8 (2020) 13793–13804, <https://doi.org/10.1021/acssuschemeng.0c04966>.
- [17] L. Wu, L. Yu, F. Zhang, B. McElhenney, D. Luo, A. Karim, S. Chen, Z. Ren, Heterogeneous bimetallic phosphide Ni<sub>2</sub>P-Fe<sub>2</sub>P as an efficient bifunctional catalyst for water/seawater splitting, *Adv. Funct. Mater.* 31 (2020), 2006484, <https://doi.org/10.1002/adfm.202006484>.
- [18] X. Zou, Y. Liu, G.-D. Li, Y. Wu, D.-P. Liu, W. Li, H.-W. Li, D. Wang, Y. Zhang, X. Zou, Ultrafast formation of amorphous bimetallic hydroxide films on 3D conductive sulfide nanoarrays for large-current-density oxygen evolution electrocatalysis, *Adv. Mater.* (2017), 1700404, <https://doi.org/10.1002/adma.201700404>.
- [19] V.R. Jothi, K. Karuppasamy, T. Maiyalagan, H. Rajan, C.Y. Jung, S.C. Yi, Corrosion and alloy engineering in rational design of high current density electrodes for efficient water splitting, *Adv. Energy Mater.* 10 (2020), 1904020, <https://doi.org/10.1002/aenm.201904020>.
- [20] Y. Liu, X. Liang, L. Gu, Y. Zhang, G.D. Li, X. Zou, J.S. Chen, Corrosion engineering towards efficient oxygen evolution electrodes with stable catalytic activity for over 6000 h, *Nat. Commun.* 9 (2018) 2609, <https://doi.org/10.1038/s41467-018-05019-5>.
- [21] F. Endres, A. Abbott, D.R. MacFarlane, *Electrodeposition from Ionic Liquids*, John Wiley & Sons, 2017.

[22] M. Gorlin, P. Chernev, J. Ferreira de Araujo, T. Reier, S. Dresp, B. Paul, R. Krahnert, H. Dau, P. Strasser, Oxygen evolution reaction dynamics, Faradaic charge efficiency, and the active metal redox states of Ni-Fe oxide water splitting electrocatalysts, *J. Am. Chem. Soc.* 138 (2016) 5603–5614, <https://doi.org/10.1021/jacs.6b00332>.

[23] M. Guo, Z. Wei, Q. Zhang, Electrochemical construction of S-doped  $\text{MnO}_x/\text{Mn}$  integrated film on carbon paper in a choline chloride based deep eutectic solvent for enhanced electrochemical water oxidation, *Int. J. Hydron. Energy* 47 (2022) 6029–6043, <https://doi.org/10.1016/j.ijhydene.2021.11.230>.

[24] X. Shang, Z.Z. Liu, J.Q. Zhang, B. Dong, Y.L. Zhou, J.F. Qin, L. Wang, Y.M. Chai, C. G. Liu, Electrochemical corrosion engineering for Ni-Fe oxides with superior activity toward water oxidation, *ACS Appl. Mater. Interfaces* 10 (2018) 42217–42224, <https://doi.org/10.1021/acsmi.8b13267>.

[25] Z. Yan, H. Sun, X. Chen, H. Liu, Y. Zhao, H. Li, W. Xie, F. Cheng, J. Chen, Anion insertion enhanced electrodeposition of robust metal hydroxide/oxide electrodes for oxygen evolution, *Nat. Commun.* 9 (2018) 2373, <https://doi.org/10.1038/s41467-018-04788-3>.

[26] P. Wei, X. Sun, Q. Liang, X. Li, Z. He, X. Hu, J. Zhang, M. Wang, Q. Li, H. Yang, J. Han, Y. Huang, Enhanced oxygen evolution reaction activity by encapsulating NiFe alloy nanoparticles in nitrogen-doped carbon nanofibers, *ACS Appl. Mater. Interfaces* 12 (2020) 31503–31513, <https://doi.org/10.1021/acsmi.0c08271>.

[27] M.Y. Gao, C.B. Sun, H. Lei, J.R. Zeng, Q.B. Zhang, Nitrate-induced and *in situ* electrochemical activation synthesis of oxygen deficiencies-rich nickel/nickel (oxy) hydroxide hybrid films for enhanced electrocatalytic water splitting, *Nanoscale* 10 (2018) 17546–17551, <https://doi.org/10.1039/c8nr06459h>.

[28] C. Liang, P. Zou, A. Nairan, Y. Zhang, J. Liu, K. Liu, S. Hu, F. Kang, H.J. Fan, C. Yang, Exceptional performance of hierarchical Ni-Fe oxyhydroxide@NiFe alloy nanowire array electrocatalysts for large current density water splitting, *Energy Environ. Sci.* 13 (2020) 86–95, <https://doi.org/10.1039/c9ee02388g>.

[29] J. Chen, Q. Long, K. Xiao, T. Ouyang, N. Li, S. Ye, Z.-Q. Liu, Vertically-interlaced NiFeP/MXene electrocatalyst with tunable electronic structure for high-efficiency oxygen evolution reaction, *Sci. Bull.* 66 (2021) 1063–1072, <https://doi.org/10.1016/j.scib.2021.02.033>.

[30] G. Li, Q. Yang, J. Rao, C. Fu, S.C. Liou, G. Auffermann, Y. Sun, C. Felser, In situ induction of strain in iron phosphide ( $\text{FeP}_2$ ) catalyst for enhanced hydroxide adsorption and water oxidation, *Adv. Funct. Mater.* 30 (2020), 1907791, <https://doi.org/10.1002/adfm.201907791>.

[31] X. Lu, J. Xie, X. Chen, X. Li, Engineering MPx ( $M = \text{Fe, Co or Ni}$ ) interface electron transfer channels for boosting photocatalytic  $\text{H}_2$  evolution over g- $\text{C}_3\text{N}_4/\text{MoS}_2$  layered heterojunctions, *Appl. Catal. B* 252 (2019) 250–259, <https://doi.org/10.1016/j.apcatb.2019.04.012>.

[32] Y. Wang, M. Qiao, Y. Li, S. Wang, Tuning surface electronic configuration of NiFe LDHs nanosheets by introducing cation vacancies (Fe or Ni) as highly efficient electrocatalysts for oxygen evolution reaction, *Small* 14 (2018), e1800136, <https://doi.org/10.1002/smll.201800136>.

[33] X. Chen, M. Yu, Z. Yan, W. Guo, G. Fan, Y. Ni, J. Liu, W. Zhang, W. Xie, F. Cheng, J. Chen, Boosting electrocatalytic oxygen evolution by cation defect modulation via electrochemical etching, *CCS Chem.* 3 (2021) 675–685, <https://doi.org/10.31635/ccschem.020.202000194>.

[34] Y. Dou, C.T. He, L. Zhang, H. Yin, M. Al-Mamun, J. Ma, H. Zhao, Approaching the activity limit of  $\text{CoSe}_2$  for oxygen evolution via Fe doping and Co vacancy, *Nat. Commun.* 11 (2020) 1664, <https://doi.org/10.1038/s41467-020-15498-0>.

[35] L. Zhuang, L. Ge, Y. Yang, M. Li, Y. Jia, X. Yao, Z. Zhu, Ultrathin iron-cobalt oxide nanosheets with abundant oxygen vacancies for the oxygen evolution reaction, *Adv. Mater.* 29 (2017), <https://doi.org/10.1002/adma.201606793>.

[36] X. He, B. Liu, S. Zhang, H. Li, J. Liu, Z. Sun, H. Chang, Nickel nitrate hydroxide holey nanosheets for efficient oxygen evolution electrocatalysis in alkaline condition, *Electrocatalysis* (2021) 37–46, <https://doi.org/10.1007/s12678-021-00686-3>.

[37] B. Liu, Y. Wang, H.Q. Peng, R. Yang, Z. Jiang, X. Zhou, C.S. Lee, H. Zhao, W. Zhang, Iron vacancies induced bifunctionality in ultrathin ferroxyhyte nanosheets for overall water splitting, *Adv. Mater.* (2018), e1803144, <https://doi.org/10.1002/adma.201803144>.

[38] L. Peng, N. Yang, Y. Yang, Q. Wang, X. Xie, D. Sun-Waterhouse, L. Shang, T. Zhang, G.I.N. Waterhouse, Atomic cation-vacancy engineering of NiFe-layered double hydroxides for improved activity and stability towards the oxygen evolution reaction, *Angew. Chem. Int. Ed. Engl.* (2021) 24817–24824, <https://doi.org/10.1002/anie.202109938>.

[39] P. Gao, Z. Chen, Y. Gong, R. Zhang, H. Liu, P. Tang, X. Chen, S. Passerini, J. Liu, The role of cation vacancies in electrode materials for enhanced electrochemical energy storage: synthesis, advanced characterization, and fundamentals, *Adv. Energy Mater.* 10 (2020), 1903780, <https://doi.org/10.1002/aem.201903780>.

[40] Y.J. Wu, J. Yang, T.X. Tu, W.Q. Li, P.F. Zhang, Y. Zhou, J.F. Li, J.T. Li, S.G. Sun, Evolution of cationic vacancy defects: a motif for surface restructuration of OER precatalyst, *Angew. Chem. Int. Ed. Engl.* (2021) 26829–26836, <https://doi.org/10.1002/anie.202112447>.

[41] S. Lee, L. Bai, X. Hu, Deciphering iron-dependent activity in oxygen evolution catalyzed by nickel-iron layered double hydroxide, *Angew. Chem. Int. Ed. Engl.* 59 (2020) 8072–8077, <https://doi.org/10.1002/anie.201915803>.

[42] A. Zagalskaya, V. Alexandrov, Role of defects in the interplay between adsorbate evolving and lattice oxygen mechanisms of the oxygen evolution reaction in  $\text{RuO}_2$  and  $\text{IrO}_2$ , *ACS Catal.* 10 (2020) 3650–3657, <https://doi.org/10.1021/acscatal.9b05544>.

[43] L. Zhang, S. Jiao, X. Tan, Y. Yuan, Y. Xiang, Y.-J. Zeng, J. Qiu, P. Peng, S.C. Smith, H. Huang, Theory-guided construction of electron-deficient sites via removal of lattice oxygen for the boosted electrocatalytic synthesis of ammonia, *Nano Res.* 14 (2020) 1457–1464, <https://doi.org/10.1007/s12274-020-3202-1>.

[44] G.H. Mhlongo, K. Shingange, Z.P. Tshabalala, B.P. Dhonge, F.A. Mahmoud, B. W. Mwakikunga, D.E. Motaung, Room temperature ferromagnetism and gas sensing in  $\text{ZnO}$  nanostructures: influence of intrinsic defects and Mn, Co, Cu doping, *Appl. Surf. Sci.* 390 (2016) 804–815, <https://doi.org/10.1016/j.apsusc.2016.08.138>.

[45] H. Che, L. Liu, G. Che, H. Dong, C. Liu, C. Li, Control of energy band, layer structure and vacancy defect of graphitic carbon nitride by intercalated hydrogen bond effect of  $\text{NO}_3^-$  toward improving photocatalytic performance, *Chem. Eng. J.* 357 (2019) 209–219, <https://doi.org/10.1016/j.cej.2018.09.112>.

[46] B. Ravel, M. Newville, ATHENA, ARTEMIS, HEPHAESTUS: data analysis for X-ray absorption spectroscopy using IFEFFIT, *J. Synchrotron Radiat.* 12 (2005) 537–541, <https://doi.org/10.1107/S0909049505012719>.

[47] H. Funke, A.C. Scheinost, M. Chukalina, Wavelet analysis of extended x-ray absorption fine structure data, *Phys. Rev. B* 71 (2005), 094110, <https://doi.org/10.1103/PhysRevB.71.094110>.

[48] K. Zhu, X. Zhu, W. Yang, Application of *in situ* techniques for the characterization of NiFe-based oxygen evolution reaction (OER) electrocatalysts, *Angew. Chem. Int. Ed. Engl.* 58 (2019) 1252–1265, <https://doi.org/10.1002/anie.201802923>.

[49] J. An, T. Shen, W. Chang, Y. Zhao, B. Qi, Y.-F. Song, Defect engineering of NiCo-layered double hydroxide hollow nanocages for highly selective photoreduction of  $\text{CO}_2$  to  $\text{CH}_4$  with suppressing  $\text{H}_2$  evolution, *Inorg. Chem. Front.* 8 (2021) 996–1004, <https://doi.org/10.1039/d0qi01259a>.

[50] D. Guo, Z. Zeng, Z. Wan, Y. Li, B. Xi, C. Wang, A CoN-based OER electrocatalyst capable in neutral medium: atomic layer deposition as rational strategy for fabrication, *Adv. Funct. Mater.* 31 (2021), 2101324, <https://doi.org/10.1002/adfm.202101324>.

[51] F. Le Formal, N. Tétreault, M. Cornuz, T. Moehl, M. Grätzel, K. Sivula, Passivating surface states on water splitting hematite photoanodes with alumina overlayers, *Chem. Sci.* 2 (2011) 737–743, <https://doi.org/10.1039/c0sc00578a>.

[52] J. Chen, J. Liu, J.-Q. Xie, H. Ye, X.-Z. Fu, R. Sun, C.-P. Wong, Co-Fe-P nanotubes electrocatalysts derived from metal-organic frameworks for efficient hydrogen evolution reaction under wide pH range, *Nano Energy* 56 (2019) 225–233, <https://doi.org/10.1016/j.nanoen.2018.11.051>.

[53] Z.R.L. Yu, Systematic study of the influence of iR compensation on water electrolysis, *Mater. Today Phys.* (2020), 100253, <https://doi.org/10.1016/j.mtphys.2020.100253>.

[54] R.L. Doyle, I.J. Godwin, M.P. Brandon, M.E. Lyons, Redox and electrochemical water splitting catalytic properties of hydrated metal oxide modified electrodes, *Phys. Chem. Chem. Phys.* 15 (2013) 13737–13783, <https://doi.org/10.1039/c3cp51213d>.